Wave effects on hinged bodies
Part IV – vertical bending modes

J. N. NEWMAN

September 11, 1998

1 INTRODUCTION

In the technical development of mobile offshore bases, one of the important hydrodynamic issues is the interaction between waves and structural deflection of the modules. It is obvious that the waves will cause structural loading on the modules, and resultant deflections, but it is not so clear if these deflections will be significant from the hydrodynamic standpoint. This question is addressed in the present work, which extends the computational analysis reported in Parts 1-3. There the modules were assumed to be rigid and computations were performed for the vertical motions and shear forces acting on the hinges.

Here we assume that the deflection of each module is governed by the beam equation, and computations are performed to show how different values of the stiffness affect the vertical motions, shear forces, and deflection of each module. As in the earlier work, each module is assumed to be a rectangular 'barge' with length 1200 feet, beam 500', and draft 20'. The modules are connected by simple hinges, with no gaps between adjacent modules. The structural deflection along the length of each module is assumed to be vertical, and independent of the transverse coordinates. The mass distribution and stuctural stiffness are assumed to be uniform along the length of each module.

As in Part 3, the computations are performed with the program HIPAN. This is a higher-order panel code which uses continuous B-splines to represent the velocity potential and pressure acting on the body surface [1]. The body geometry is described exactly. HIPAN has been extended to permit the definition and use of generalized modes, which are employed here to represent the hinge deflections as defined in Part 1, and discontinuous shear modes which are used to evaluate the shear forces on the hinges, as described in Part 2. In addition we now include a set of Fourier modes which represent the vertical bending deflection of each module. In order to achieve computational efficiency these bending modes are decomposed into pairs of components which are respectively symmetrical and antisymmetrical about the middle of the array.

As in the earlier work, a Cartesian coordinate system (x, y, z) is used with $z = 0$ the undisturbed free surface, x positive toward the 'bow' of the array, y positive toward the port side of the array, and z positive upwards. Each module is considered to be an identical floating vessel with geometric symmetry about the vertical centerplane $y = 0$ and also about its midship section. The origin $x = 0$ is at the midpoint of the array. Simple transverse hinge joints are located at $x = x_n$ $(n = 1, 2, ..., N - 1)$. These are numbered in ascending order from the stern $(x = x_0)$ to the bow $(x = x_N)$. The overall length L of each module is defined as the distance between adjacent hinges, $x_{n+1} - x_n$. As in Part 1 we assume that the hinge axes are in the plane $z = 0$, and we neglect surge.

In general the motions of the array will include six conventional rigid-body modes (surge, sway, heave, roll, pitch, yaw) where the entire array is translating and rotating as a rigid body, and $N - 1$ additional modes corresponding to deflections of the hinges. Since the array geometry is symmetric about $y = 0$, there is no coupling between the vertical motions considered here (heave, pitch, and hinge deflections) and the sway, roll, and yaw motions. Similarly, the vertical bending displacement of each module is coupled with the vertical modes, but not with sway, roll or yaw. Thus we shall ignore the latter three modes.

It should be noted that horizontal bending and torsional deflection of the array will also occur, in general. Complementing the symmetric modes described above, these antisymmetrical structural deflections are coupled to sway, roll, and yaw, but not to surge, heave or pitch. Thus the horizontal bending and torsional deflections can be analyzed separately from the present analysis, using similar computational methods.

In addition to the assumptions noted above, we assume that the array of modules is unrestrained, with hydrostatic equilibrium in its mean position when no waves are present and with positive stability in the vertical modes. Thus the submerged volume of each module is equal to the ratio M/ρ where M is its mass and ρ the fluid density. The analysis which follows considers only the linearized oscillatory perturbations about this mean equilibrium.

2 ANALYSIS OF BENDING DEFLECTIONS

The vertical displacement at a position x along the array, due to the superposition of all vertical motions and bending deflections, is defined in the form $\mathrm{Re}\left(\xi(x)\,\mathrm{e}^{i\omega t}\right)$. This displacement is continuous along the array, and governed by the beam equation

$$-\omega^2 m\xi + (EI\xi'')'' = Z(x), \tag{2.1}$$

Here $m(x)$ is the mass per unit length, E is the modulus of elasticity, and I denotes the moment of inertia for the cross-sectional area of the structure.

Primes denote differentiation with respect to x, and $Z(x)$ is the local pressure force acting on a vertical section of unit length along the array.

The appropriate boundary conditions imposed on the structure are that (i) the structural moment vanishes at the two ends and also at each hinge:

$$(EI\xi'') = 0, \qquad x = x_n \quad (n = 0, 1, 2, ..., N), \tag{2.2}$$

(ii) the shear force vanishes at the two ends:

$$(EI\xi'')' = 0, \qquad x = x_0,\ x = x_N, \tag{2.3}$$

and (iii) the shear force is continuous between adjacent modules:

$$\Big[(EI\xi'')'\Big]_-^+ = 0, \qquad x = x_n \quad (n = 1, 2, ..., N-1). \tag{2.4}$$

The left hand side of (2.4) denotes the difference in the shear force across the hinge.

The displacement ξ may be expanded in an appropriate set of modes, in the form

$$\xi(x) = \sum_j \xi_j f_j(x), \tag{2.5}$$

where the (complex) amplitude ξ_j of each mode is unknown. The appropriate modes will include heave and pitch of the entire array, moving as a rigid body, and $N-1$ hinge deflections, as defined in Part 1. In addition we now include a suitable set of modal functions to represent the bending deflection of each module. Since the vertical displacement of each hinge is represented by the preceding modes, the bending modes are defined such that these vanish at the ends of the module, and on all other modules. In addition to these modes, which represent the actual physical displacement of the array, $N-1$ discontinuous shear modes will also be used, as in Part 2, to evaluate the vertical shear forces acting on the hinges.

Adopting the method of weighted residuals as in [2], (2.1) is multiplied by $f_i(x)$ and integrated along the length, to give the system of equations

$$\sum_{n=1}^{N} \int_{x_{n-1}}^{x_n} f_i(x)\big[-\omega^2 m\xi(x) + \big(EI\xi''(x)\big)''\big]dx = \sum_{n=1}^{N} \int_{x_{n-1}}^{x_n} f_i(x) Z(x) dx. \tag{2.6}$$

Note that we have not yet approximated $\xi(x)$ in terms of its modal expansion. Before doing so, we consider the stiffness term, which can be integrated by parts two times. It follows that

$$\begin{aligned}\textstyle\sum_{n=1}^{N} \int_{x_{n-1}}^{x_n} f_i(x)\big(EI\xi''(x)\big)'' dx &= \textstyle\sum_{n=1}^{N} \int_{x_{n-1}}^{x_n} f_i''(x)\big(EI\xi''(x)\big) dx \\ &+ \textstyle\sum_{n=1}^{N-1} \Big[f_i(x)\big(EI\xi''(x)\big)' - f_i'(x)\big(EI\xi''(x)\big)\Big]_-^+ \end{aligned} \tag{2.7}$$

The contributions from the last pair of terms vanish at the two ends, as in the usual case of a single beam, in view of the boundary conditions (2.2) and (2.3).

In addition, since the modes f_i and shear force $\left(EI\xi''(x)\right)'$ are both continuous at each hinge, and the moment vanishes, the contributions from the last pair of terms in (2.7) also vanish at the hinges. (Continuity of the bending modes is required, but the first derivatives can be discontinuous. When discontinuous shear modes are used to evaluate the hinge shear loads, as in Section 3 of Part 2, the required shear load component is equal to the non-vanishing contribution from the first term on the last line of equation 2.7.) Thus (2.6) can be replaced by

$$\sum_{n=1}^{N}\int_{x_{n-1}}^{x_n}\left[-\omega^2 m f_i(x)\xi(x) + EIf_i''(x)\xi''(x)\right]dx = \sum_{n=1}^{N}\int_{x_{n-1}}^{x_n} f_i(x)Z(x)dx. \quad (2.8)$$

At this point (2.5) is substituted for $\xi(x)$, and the conventional linear system follows in the form

$$\sum_j \xi_j\left[-\omega^2 M_{ij} + C_{ij}\right] = \sum_{n=1}^{N}\int_{x_{n-1}}^{x_n} f_i(x)Z(x)dx, \quad (2.9)$$

where the coefficients on the left-hand-side are the mass matrix

$$M_{ij} = \sum_{n=1}^{N}\int_{x_{n-1}}^{x_n} m f_i(x)f_j(x)dx \quad (2.10)$$

and the stiffness matrix

$$C_{ij} = \sum_{n=1}^{N}\int_{x_{n-1}}^{x_n} EIf_i''(x)f_j''(x)dx. \quad (2.11)$$

The hydrodynamic and hydrostatic coefficients on the right-hand-side of (2.9) are evaluated by HIPAN, to give the added mass, damping, hydrostatic restoring, and exciting forces and moments corresponding to each of the modes. The program also will evaluate the response-amplitude operator (RAO) in each mode, provided the mass and stiffness matrices (2.10-11) are input.

3 DEFINITION OF THE BENDING MODES

We now consider the explicit definitions of the bending modes, in terms of a separate Fourier sine series for each module. For this purpose it is helpful to define the normalized local coordinate

$$u = (x - x_{n-1})/L \quad (3.1)$$

associated with the interval $(x_{n-1} < x < x_n)$. Along the length of each module u increases from 0 to 1. Since the structural deflections vanish at the end points, an appropriate set of modes are defined by

$$\hat{f}_n^{(m)}(u) = \sin(m\pi u) \qquad (n = 1, 2, ..., N;\ m = 1, 2, ..., M) \quad (3.2)$$

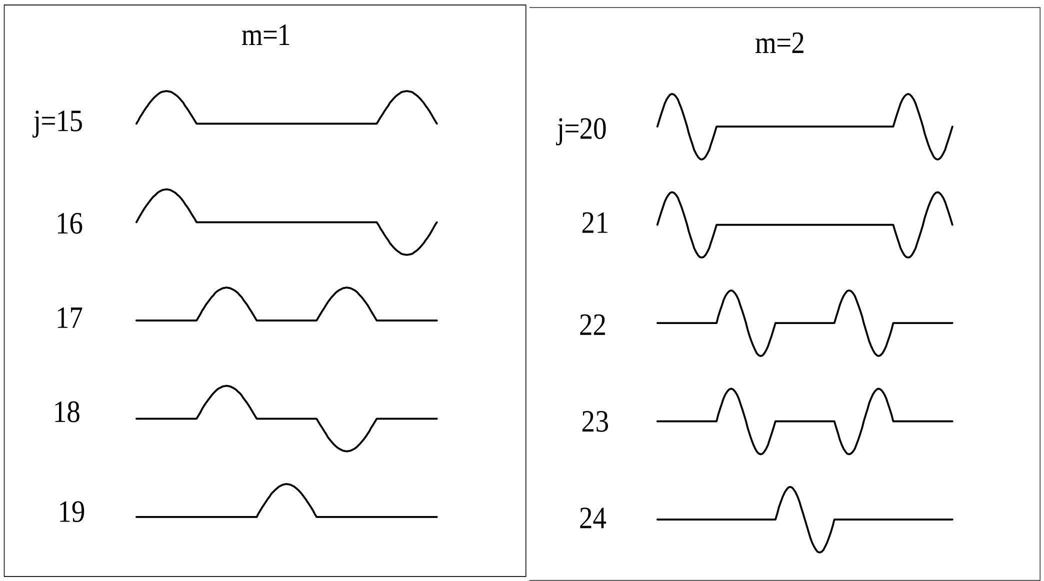

Figure 1: The first ($m = 1$) and second ($m = 2$) bending modes for the array with $N = 5$ modules.

with the understanding that $\hat{f}_n(u) = 0$ when $x < x_{n-1}$ or $x > x_n$. In principle an infinite number M of these modes is required on each module, but an arbitrary degree of numerical accuracy can be achieved by truncating the set at a sufficiently large finite integer $m = M$. While it is not strictly necessary for the separate modes to satisfy the boundary conditions (2.2-4), we note that (2.2) is in fact satisfied by (3.2).

Symmetric and antisymmetric modes are constructed in the forms

$$f_j(u) = \hat{f}_n^{(m)}(u) + \hat{f}_{N+1-n}^{(m)}(u) \qquad (n = 1, 2, ..., [N/2]) \tag{3.3}$$

$$f_j(u) = \hat{f}_n^{(m)}(u) - \hat{f}_{N+1-n}^{(m)}(u) \qquad (n = 1, 2, ..., [N/2]) \tag{3.4}$$

When N is odd the additional modes

$$f_j(u) = \hat{f}_n^{(m)}(u) \qquad (n = (N+1)/2)) \tag{3.5}$$

must be included, to account for the deflection of the middle module.

The index j in (3.3-5) is assigned following the rigid-body modes ($j = 1-6$), the hinge modes ($j = 7, ..., N+5$), and the shear modes ($j = N+6, ..., 2N+4$). Thus

$$j = N(m+1)+5, N(m+1)+7, ..., N(m+1)+2[N/2]+3 \qquad \text{modes (3.3)}$$

$$j = N(m+1)+6, N(m+1)+8, ..., N(m+1)+2[N/2]+4 \qquad \text{modes (3.4)}$$

$$j = N(m+2)+4 \qquad (N = \text{odd}) \qquad \text{mode (3.5)}$$

Figure 1 shows the first two Fourier modes for each module, with the corresponding index j, for the case $N = 5$.

With the bending modes defined as above, the only nonzero integrals in (2.11) are on the diagonal ($i = j$) for $j \geq 2N + 5$. For the modes defined by (3.3) and (3.4) the stiffness coefficients have the following values:

$$C_{jj} = \pi^4 m^4 EI/L^3 \qquad (j \geq 2N + 5) \tag{3.6}$$

For the middle module when N is odd, corresponding to the modes (3.5),

$$C_{jj} = \tfrac{1}{2}\pi^4 m^4 EI/L^3 \qquad (j = N(m+2) + 4),\ (N = \text{odd}) \tag{3.7}$$

It is convenient to define the nondimensional stiffness coefficient $S = EI/\rho g L^5$, where ρ is the fluid density, g gravity, and L is the length of each module. From the physical standpoint, this coefficient represents the ratio between the structural stiffness and the hydrostatic restoring force.

4 HYDRODYAMIC COEFFICIENTS

Figure 2 shows the computed values of the hydrodynamic coefficients for each mode, at the wave period $T = 12$ seconds, to illustrate the relative importance of different modes. For this purpose the added-mass coefficients are normalized by the total mass of the array, except for the pitch mode ($j = 5$) where the second moment of inertia is used. The damping coefficients are normalized by the same factors, and by the frequency ω. The exciting-force coefficients and response-amplitude operators (RAO) are for head seas, and show the moduli of the corresponding complex quantities. The normalization factor for the exciting force is the product of the fluid density ρ, gravity g, wave amplitude A, and the area of the waterplane (waterplane moment of inertia for $j = 5$). The RAO's are normalized by the wave amplitude, except for $j = 5$ which represents the pitch angle in degrees per unit wave amplitude in feet. For the RAO evaluations the nondimensional stiffness factor $S = 0$ is used, corresponding to the case where the barges are completely flexible.

In the interpretation of these results we note first that the wavelength corresponding to $T = 12$ seconds is equal to 737 feet, hence there are approximately 8 waves along the length of the array. Since there is no structural stiffness the barges are expected to deflect locally in phase with the incident wave, and this will be confirmed in the next Section. This limiting case is a stringent test of the numerical accuracy, since a relatively large number of modes are required to represent the oscillatory motion along the array. The trend of the RAO with increasing mode index suggests that the truncation error in (2.5) is of order 10^{-2}.

The added-mass and damping coefficients are relatively large for the rigid-body modes $j = 3, 5$ and (to a slightly less extent) also for the hinge modes. This is expected for the vertical motion of a floating body with large waterplane area and small draft. For the bending modes these coefficients diminish rapidly with

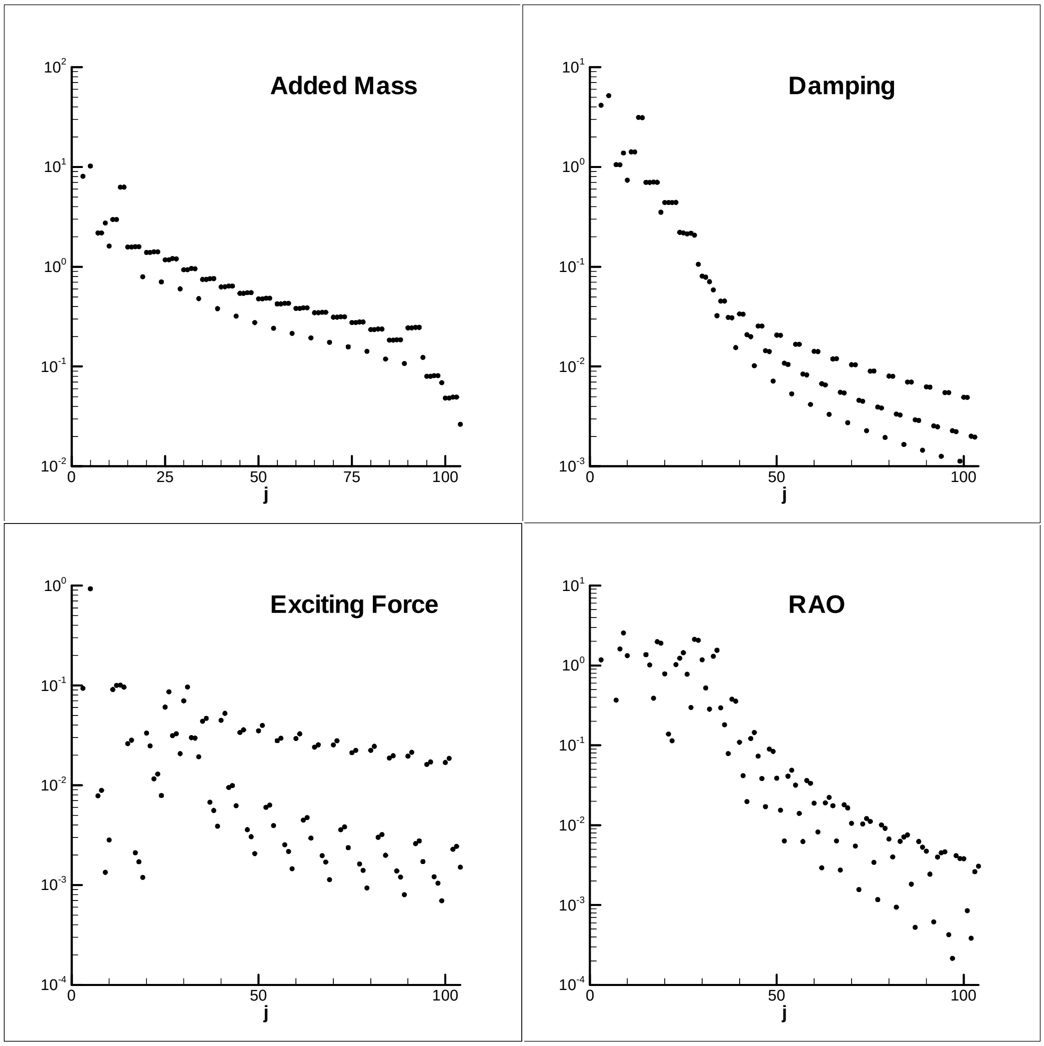

Figure 2: Normalized values of the hydrodynamic coefficients for each mode index j. The wave period $T = 12$ seconds. In the lower figures the moduli of the complex exciting-force coefficients and RAO's are plotted, for head seas, and the stiffness factor $S = 0$ is used for the RAO's. The attenuation of the added-mass coefficients for $j > 90$ is a numerical error caused by an insufficient number of longitudinal panels, as explained in Section 9.

increasing Fourier index m, due to hydrodynamic cancelation along the length associated with the oscillatory modes. The attenuation of the damping is greater than for the added mass, since the energy radiated to the far field is reduced. [Radiated waves moving away from the body in the far field, propagating in the direction θ relative to the $x-$axis, are of the form $\exp(iKx\cos\theta \pm iKy\sin\theta)$ where $K = \omega^2/g$ is the wavenumber. Assuming a long slender body and an oscillatory mode of motion proportional to $\exp(ikx)$, radiation in the near field of the body can only occur if $k < K$. For the complete three-dimensional solution this near-field analysis is not strictly valid, but it does explain qualitatively the fact that the damping is small compared to the added mass when the Fourier mode index m is large.]

All three of the force coefficients display a grouping of the bending modes in sets of five, corresponding to the different modes shown in Figure 1. For the exciting force one pair of coefficients is relatively large. These correspond to the symmetric and antisymmetric modes of the end modules. The forces acting on the interior three modules are much smaller. The pair of modes for the end modules have opposite phase, cancelling at the downwave end and reinforcing at the upwave end. Thus the exciting force acting on the upwave module is much larger than the forces on the other modules, as may be expected. Similarly, the damping coefficients of the end modules are larger than the others due to the presence of the adjacent free surface at the ends.

The results shown for the added mass are attenuated, starting at about $j = 90$, due to using an insufficient number of panels in the longitudinal direction; this numerical error, which does not affect the other coefficients in Figure 2 within graphical accuracy, is discussed further in Section 9.

5 ELEVATION ALONG THE LENGTH

Figures 3-6 show the elevation of the array along its length in head waves, for four different wave periods and six different values of the stiffness coefficient S. The elevation is normalized by the incident-wave amplitude. The solid and dashed curves correspond respectively to the real and imaginary parts of the vertical displacement $\xi(x)$. The stiffness coefficients shown cover the range from effectively rigid ($S = 0.1$) to completely flexible ($S = 10^{-6}$ to 10^{-8}). In the transition regime between $S = 10^{-3}$ and 10^{-4} hydroelastic effects are expected to be important.

In the most flexible cases ($S = 10^{-6}$ and 10^{-8}) there is a quarter-period phase difference between the real and imaginary displacements, hence the deflection is a wave-like disturbance propagating along the length of the array with the same phase velocity as the incident waves. It is interesting to note in these cases that the deflection is substantially greater than the incident wave amplitude. This amplification is due to the effect of finite draft, as explained below.

Intuitively one might expect that a floating body with no structural stiffness, and uniform mass distribution, would deform to follow precisely the incident-wave elevation. In the case of a 'mat' with zero draft this behavior was confirmed using WAMIT [3]. (This limiting case was regarded in that work as a stringent test of numerical accuracy.)

For hinged modules with zero stiffness, the hinges are irrelevant and the array will have the same vertical motions as a flexible monohull with the same overall dimensions. The plots for $S = 10^{-8}$ in Figures 3-6 confirm that the elevation follows the incident wave, with the same phase velocity and a nearly-sinusoidal form. However the amplitude is greater than the incident wave by up to 100% for wave periods of 12 and 16 seconds, decreasing to the wave amplitude asymptotically as the period increases. The same conclusions are indicated in Figures 12-13.

It may seem surprising, for a structure with horizontal dimensions 6000' by 500' in the presence of incident waves with wavelengths greater than 700', that a draft of only 20' causes such a substantial increase in the motions. In fact, the draft has no significant effect on the hydrodynamic force coefficients, on the right side of the equations of motion (2.9), but only on the mass matrix (2.10). (The stiffness matrix (2.11) is assumed to be zero in this context, and thus independent of the draft.) For the lower-order modes including heave and pitch, the added mass dominates the body mass, as illustrated in Figure 2, and the damping is substantial. However for the higher-order modes, which are important only when the stiffness is small, the added mass and damping are much smaller and the body mass is more important. (In this context it should be noted that the diagonal elements M_{ii} of the mass matrix (2.10) do not attenuate for increasing values of the Fourier mode index m.) Since the body mass is proportional to the draft, the observed results are explained.

6 ELEVATION AT THE MODULE ENDS

Figures 7-13 show the elevations at the ends of each module, including the stern, hinges, and bow, for wave periods between 6 and 30 seconds. In each plot five different wave headings are shown including 180° (head seas) and 140° to 110°, the range of oblique headings where the maximum shear forces occur on the hinges. The elevations are normalized by the incident-wave amplitude.

Stiffness coefficients from $S = 0.1$ to $S = 0$ are included. Comparison of the first two figures confirms that there is no significant effect of bending for $S \geq 10^{-2}$. Conversely, comparison of the last pair of figures confirms that $S = 10^{-8}$ is practically equivalent to the limit $S = 0$ except for the shortest wave periods, where the numerical accuracy is uncertain.

7 BENDING DEFLECTION

Figures 14-18 show the bending deflections at the midpoint of each module, normalized by the incident-wave amplitude. Stiffness parameters greater than $S = 10^{-2}$ are omitted since the corresponding deflections are not visible in the plots.

8 HINGE SHEAR FORCES

Figures 19-24 show the vertical shear force acting at each hinge. The cases $S = 10^{-1}$ and $S = 10^{-2}$ are identical except for minor differences, confirming that there are no significant effects of structural deflection on the shear forces when $S \geq 10^{-2}$. In general, for $S < 10^{-2}$, decreasing stiffness also decreases the shear forces, as one expects. However this trend is reversed for hinge 1 (nearest the stern) at $S = 10^{-3}$, for oblique wave headings and periods below 15 seconds. This suggests a structural resonance in this regime.

9 COMPUTATIONAL NOTES

The results presented here are based on computations performed with the HIPAN program. Geometric symmetry about $x = 0$ and $y = 0$ is exploited to reduce the total number of unknowns in the hydrodynamic solution. The surface of each module (in the domain $x > 0$, $y > 0$) is described exactly by flat rectangular 'patches', using one patch on the bottom, one on the side, and one patch on the end of the last module. The solution for the velocity potential is represented by B-splines in terms of orthogonal parametric coordinates which lie in each patch. The accuracy of the solution depends on the order of the B-splines, which has been set equal to 3, and on the number of subdivisions of the patches into 'panels'. Based on preliminary computations for a single module, it was found that about three decimals accuracy could be achieved using 8 longitudinal subdivisions along each module, two vertically on the sides and ends, four transversely across half of the end, and two transversely across half of the bottom. These subdivisions were used for all of the results shown, with the exception of the plots in Figure 2 which are discussed below.

The number M of Fourier bending modes on each module was initially set equal to 9, but increased to 18 to refine the results for the smallest values of the stiffness parameter. With $M = 18$ there are a total of 5×18 bending modes, in addition to the 10 modes used to represent heave, pitch, hinge motions, and hinge shear. Thus a total of 100 radiation solutions were included.

The choice of 8 longitudinal subdivisions on each module was found to affect the added-mass coefficients and RAO's shown in Figure 2. For the modes $j \geq 54$, corresponding to the Fourier index $m > 8$, the added mass was attenuated by about one decade, and the RAO's were increased by a similar factor. It is logical to expect that as the Fourier index is increased a larger number of longidutinal subdivisions will be required to adequately represent the solution. To overcome this problem the number of longitudinal subdivisions was increased to 16 per module for the results shown in Figure 2. Even with this more complete representation of the solution some attenuation is evident in the added-mass coefficients for $j \geq 90$ or $m \geq 16$. In addition to the coefficients shown in

Figure 2, the elevation along the length shown in the last plot of Figure 3 was re-computed with this more accurate solution, with no observable differences within graphical precision. Thus it is reasonable to assume that this refinement has no significant effect on any other results shown here.

Our objective in performing these computations has been to achieve an accuracy in all of the results within the graphical tolerance of the figures. The convergence tests which have been conducted suggest that this objective has been achieved in most but not all cases. The exceptions occur for the smallest values of the stiffness parameter ($S = 0$ and $S = 10^{-8}$), and for wave periods below approximately 12 seconds. In this regime 18 bending modes for each module is not sufficient, and possibly the number of panels must be increased as well if accurate results are required. Since there is little practical importance to such flexible structures, we have not attempted to refine the computations to overcome this limitation. Indeed, the main purpose for considering the cases where $S \leq 10^{-6}$ is to demonstrate that the deflections of very flexible modules follow the phase of the incident wave.

References

[1] C.-H. Lee, H. D. Maniar, J. N. Newman, & X. Zhu, 'Computations of wave loads using a B-spline panel method,' 21st Symposium on Naval Hydrodynamics, Trondheim, Norway (1996).

[2] J. N. Newman, 'Wave effects on deformable bodies,' Applied Ocean Research, Volume 16 (1994).

[3] J. N. Newman, H. D. Maniar, & C.-H. Lee, 'Analysis of wave effects for very large floating structures,' Proceeding of International Workshop on Very Large Floating Structures, Hayama, Japan (1996).

[4] C.-H. Lee, 'Wave interaction with huge floating structure,' International Conference on the Behaviour of Offshore Structures (BOSS '97), Delft, Netherlands (1997).

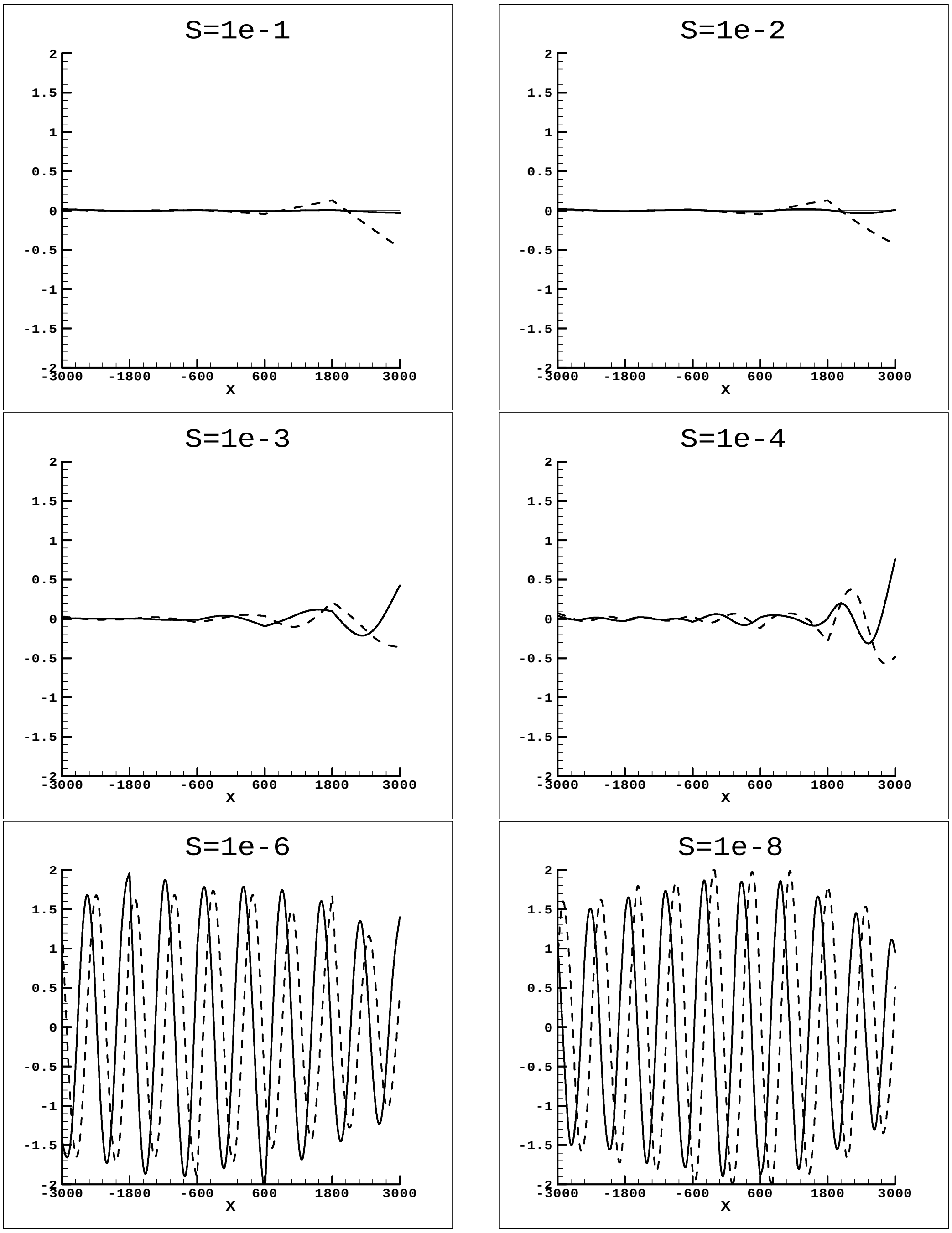

Figure 3: Elevation along the length, $T = 12$ seconds, head seas. The solid and dashed lines denote the real and imaginary parts of $\xi(x)$, respectively.

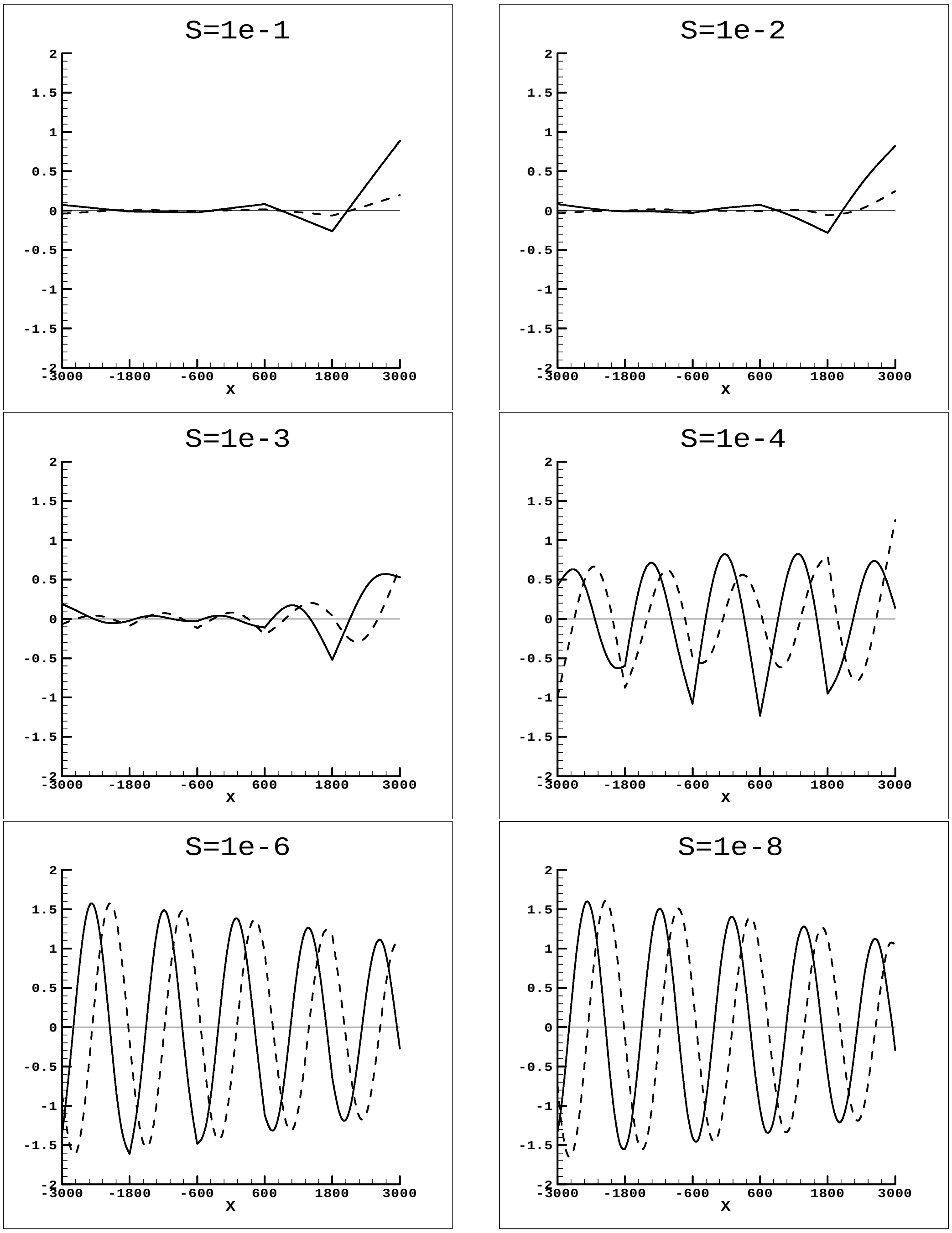

Figure 4: Elevation along the length, $T = 16$ seconds, head seas. The solid and dashed lines denote the real and imaginary parts of $\xi(x)$, respectively.

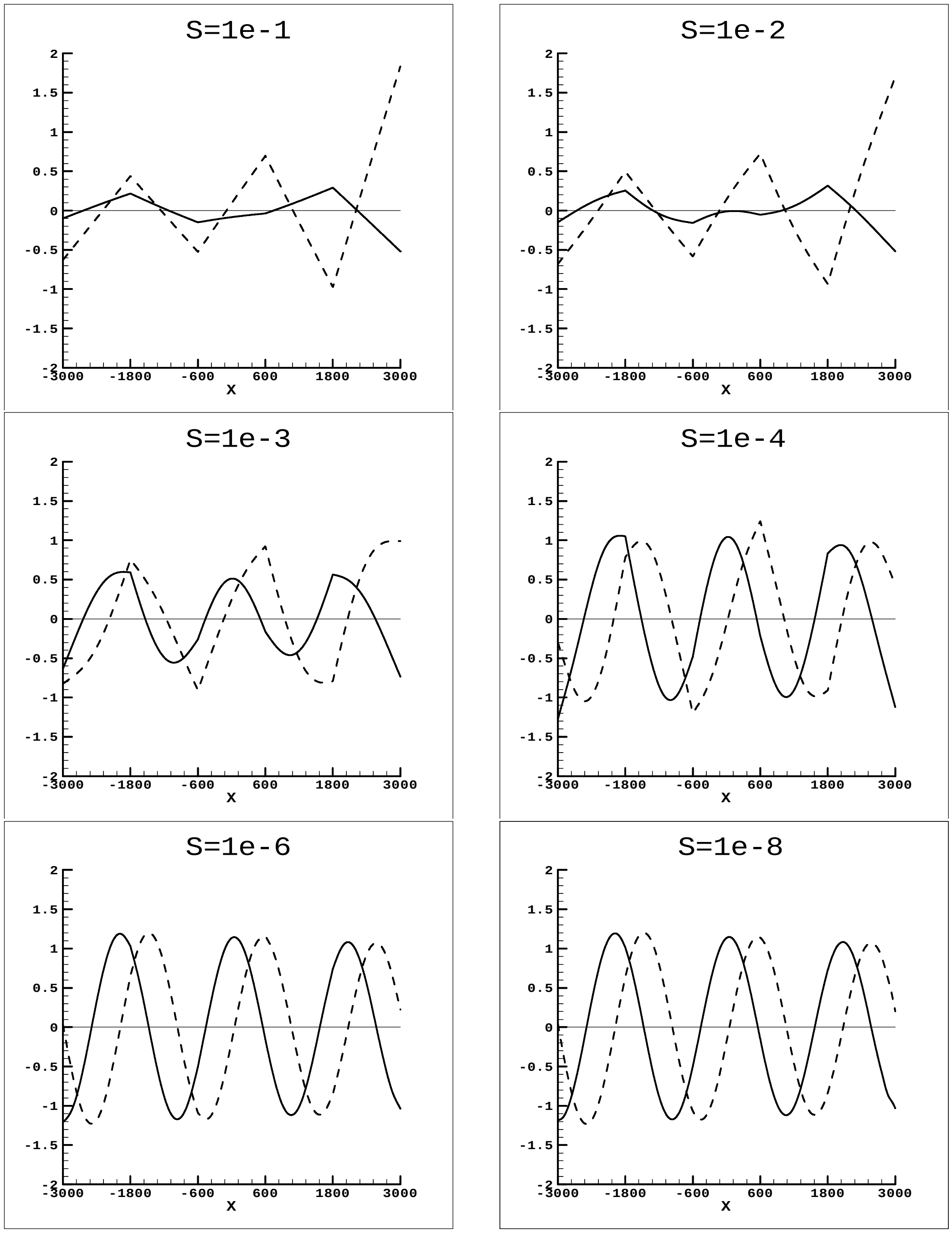

Figure 5: Elevation along the length, $T = 20$ seconds, head seas. The solid and dashed lines denote the real and imaginary parts of $\xi(x)$, respectively.

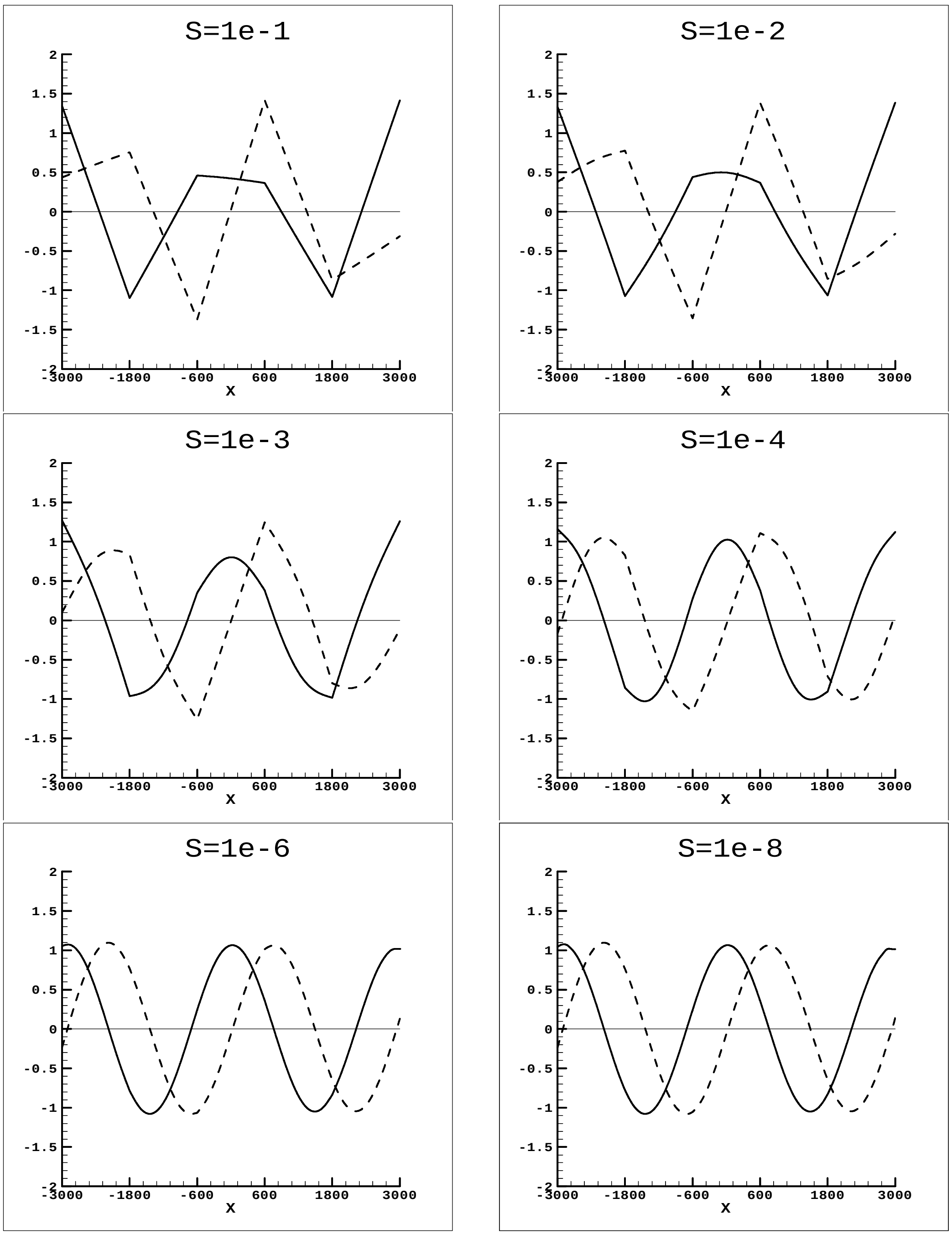

Figure 6: Elevation along the length, $T = 24$ seconds, head seas. The solid and dashed lines denote the real and imaginary parts of $\xi(x)$, respectively.

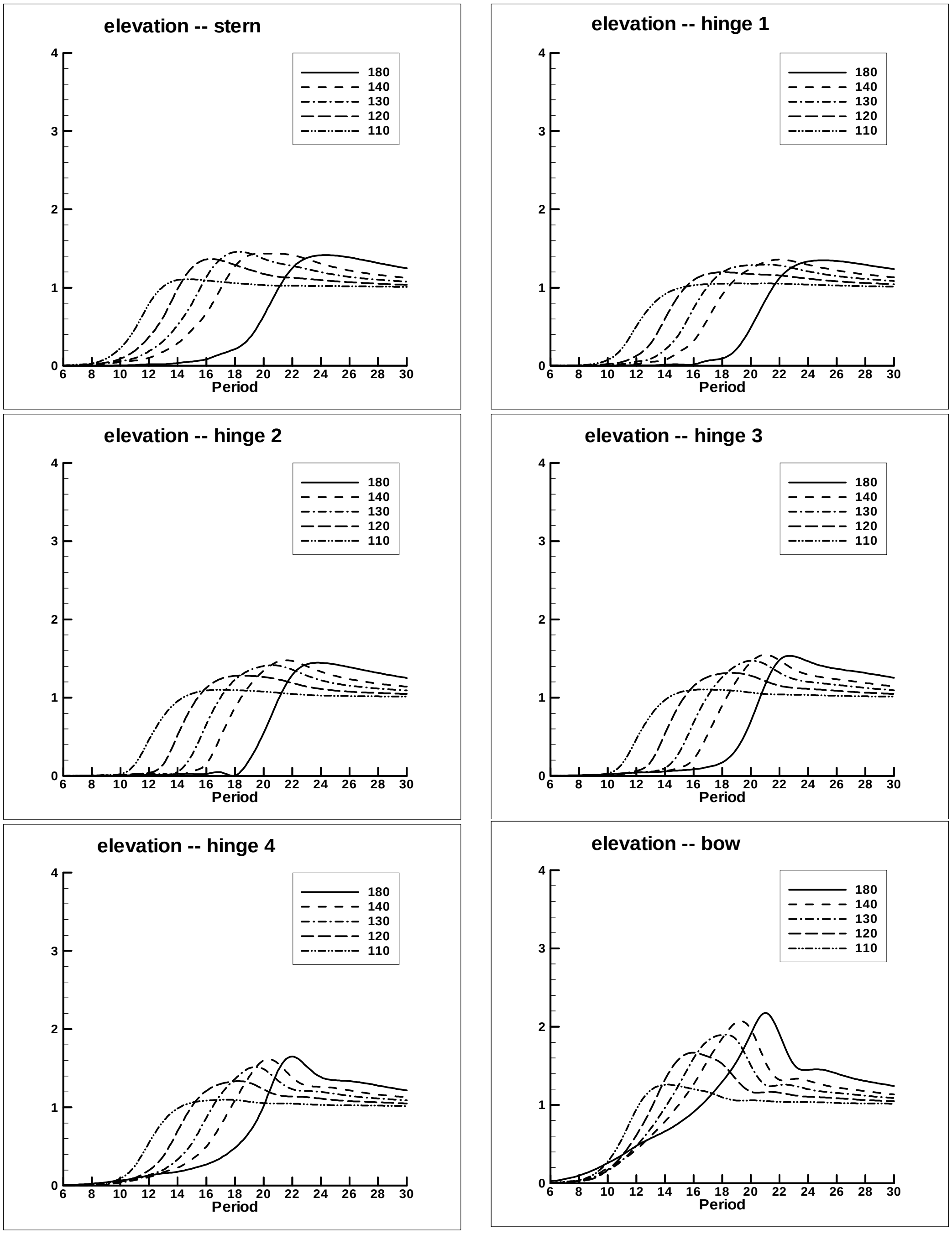

Figure 7: Elevation at the stern, hinges, and bow. Stiffness $S = 10^{-1}$. The wave headings in degrees are shown in the legend with 180° head seas.

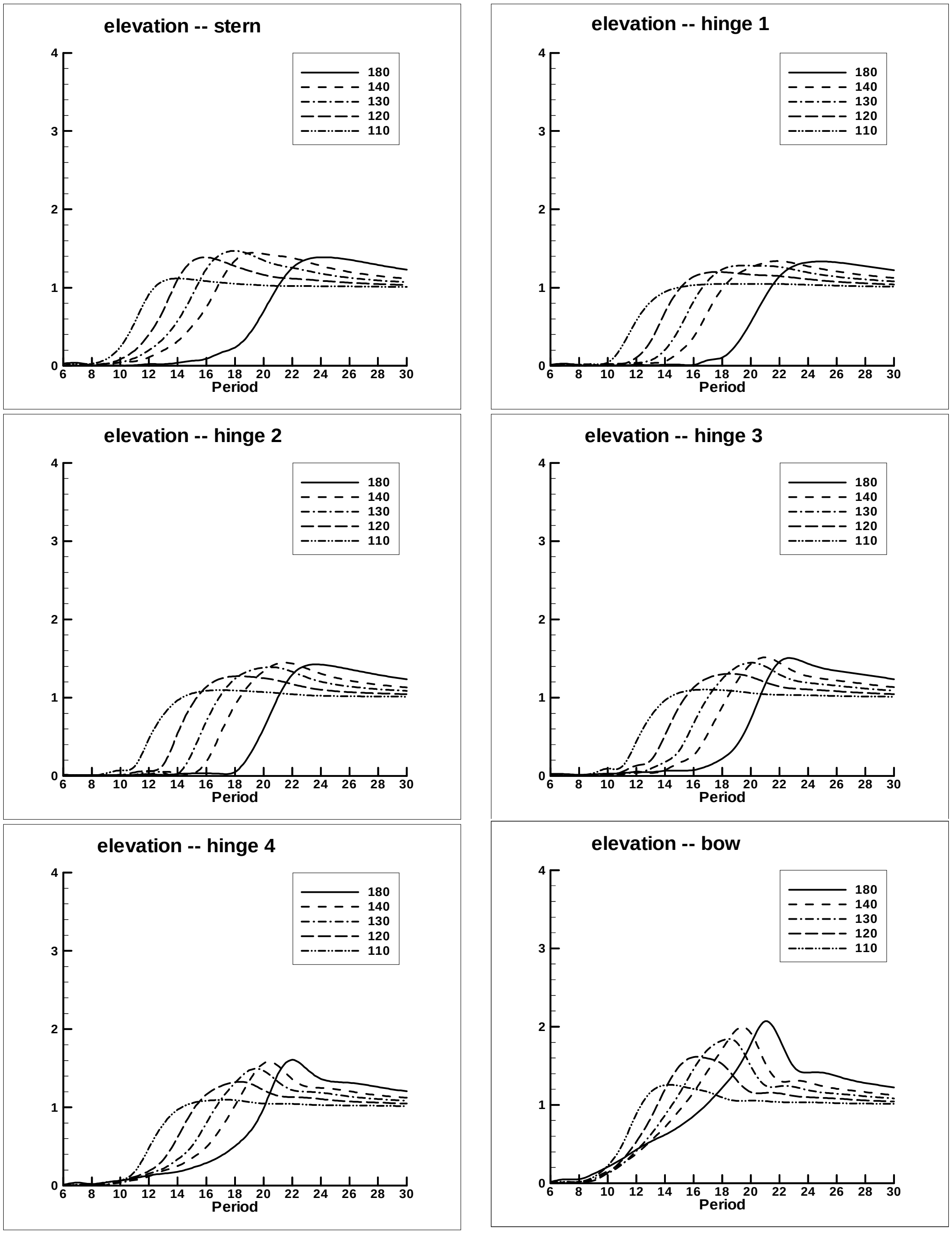

Figure 8: Elevation at the stern, hinges, and bow. Stiffness $S = 10^{-2}$. The wave headings in degrees are shown in the legend with 180° head seas.

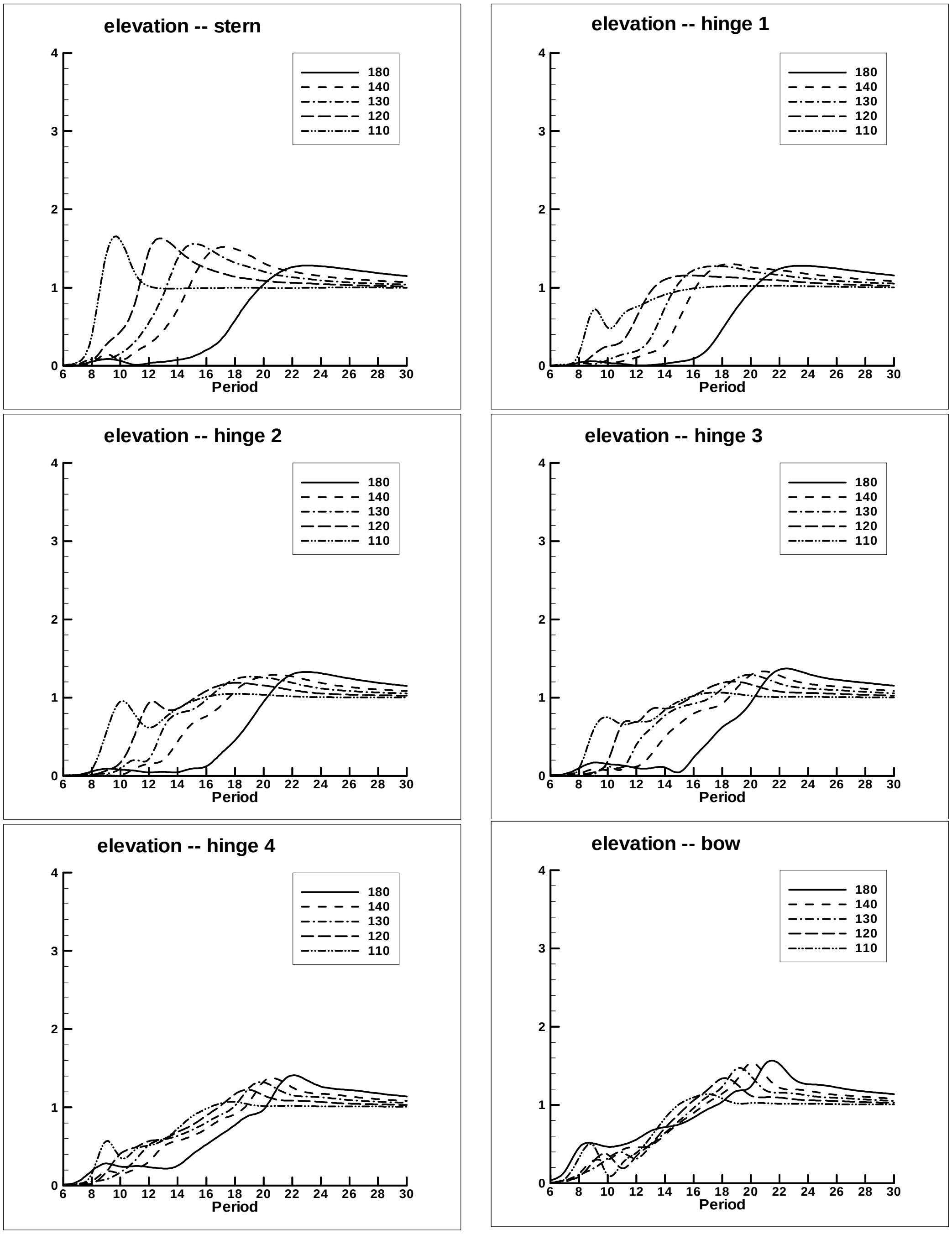

Figure 9: Elevation at the stern, hinges, and bow. Stiffness $S = 10^{-3}$. The wave headings in degrees are shown in the legend with 180° head seas.

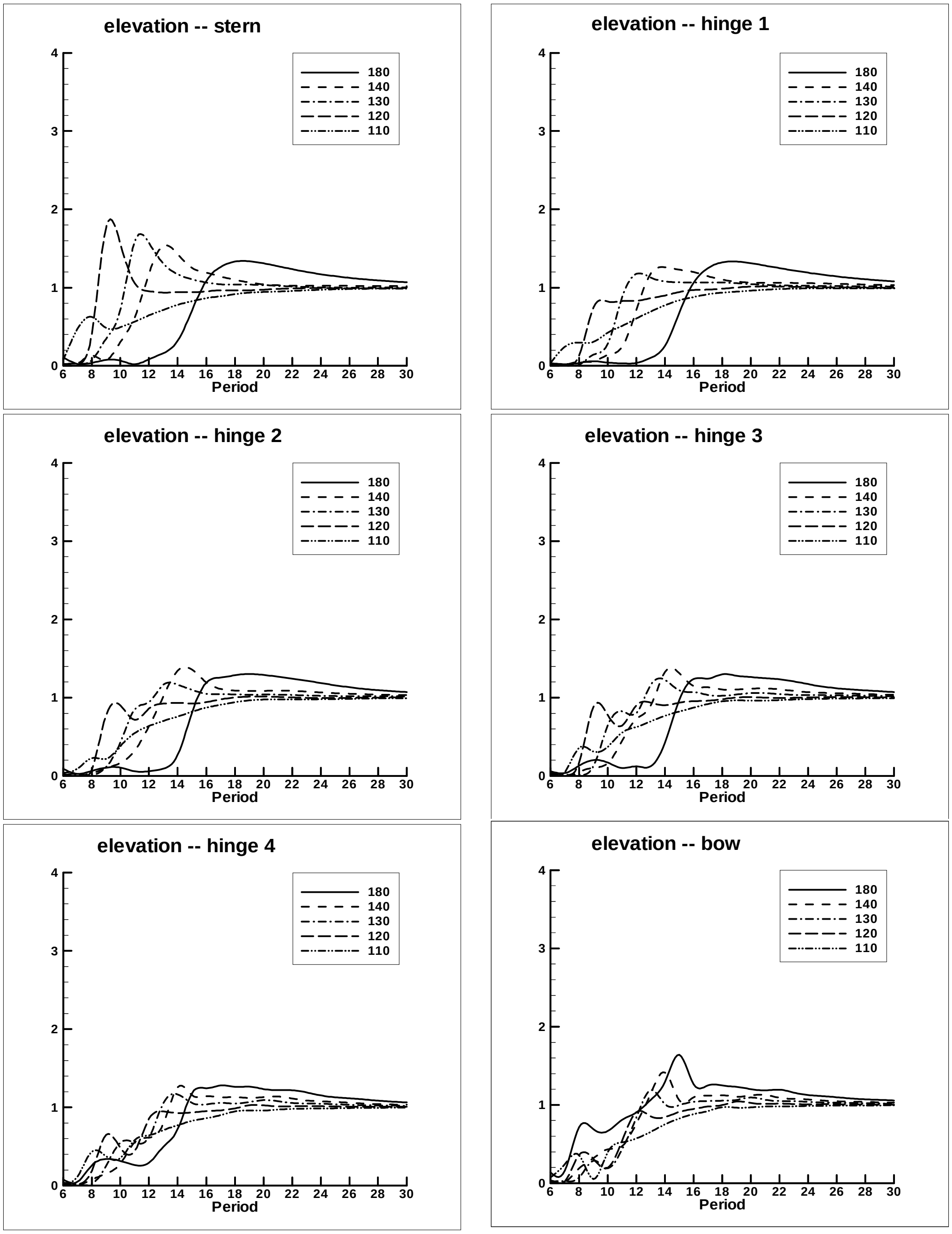

Figure 10: Elevation at the stern, hinges, and bow. Stiffness $S = 10^{-4}$. The wave headings in degrees are shown in the legend with 180° head seas.

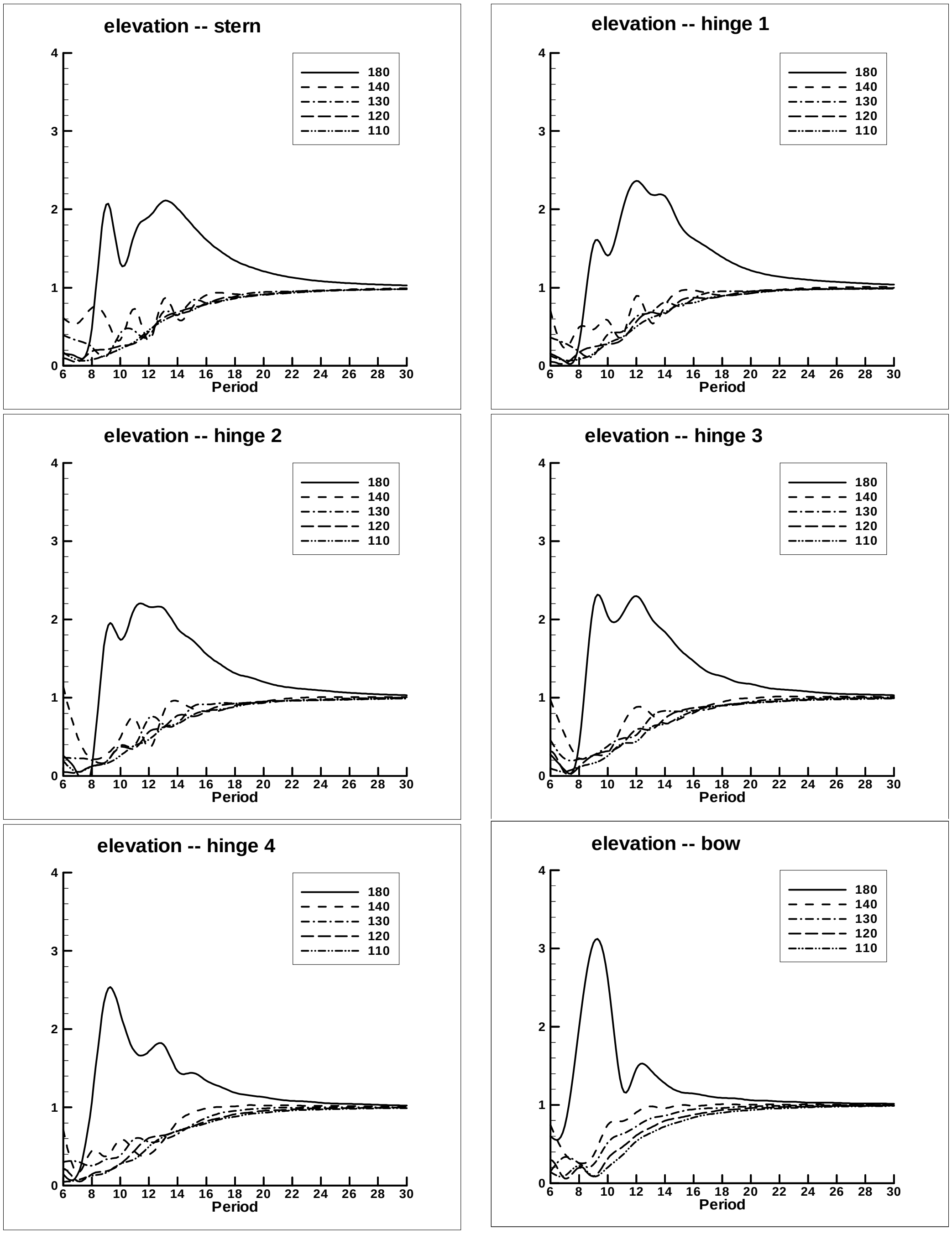

Figure 11: Elevation at the stern, hinges, and bow. Stiffness $S = 10^{-6}$. The wave headings in degrees are shown in the legend with 180° head seas.

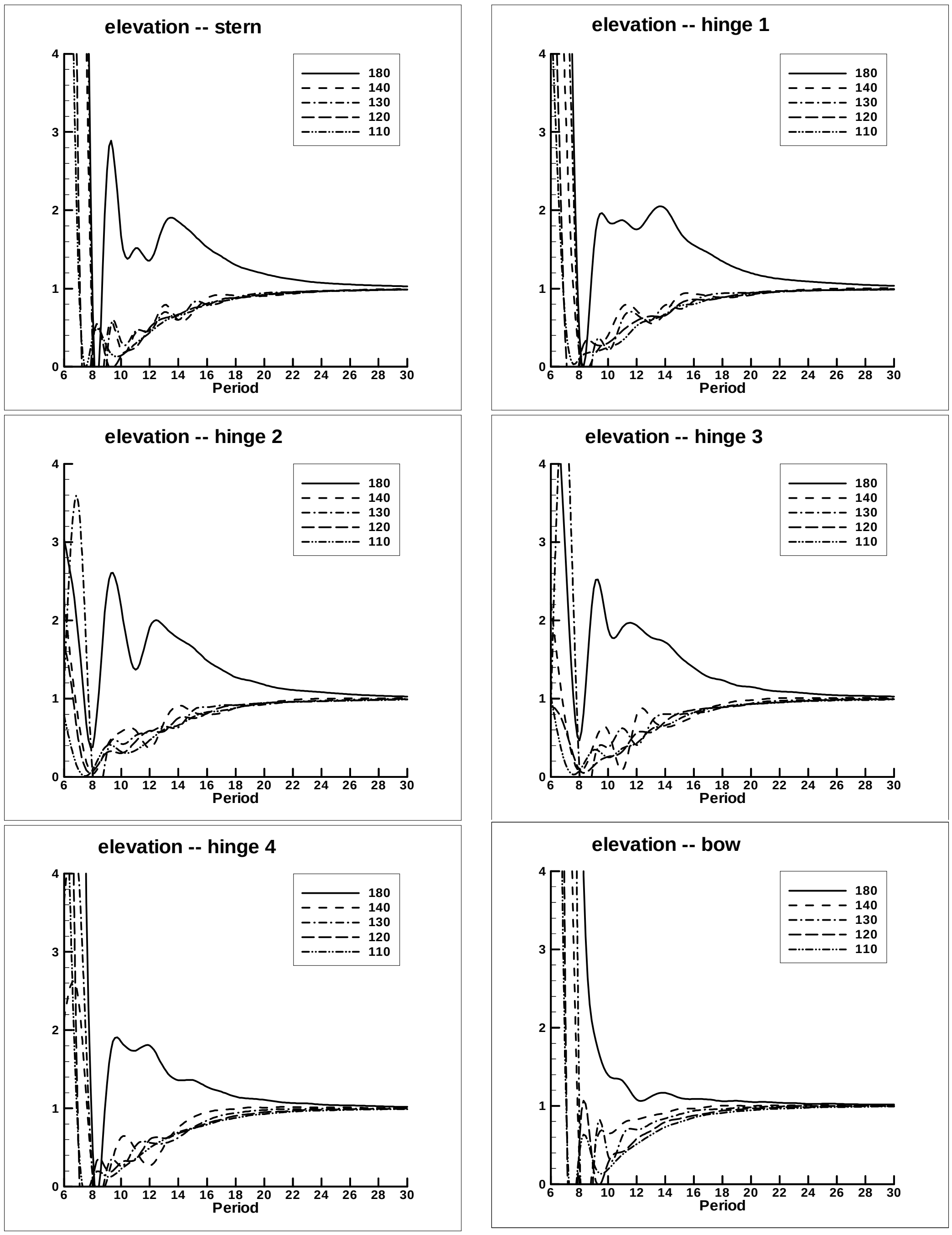

Figure 12: Elevation at the stern, hinges, and bow. Stiffness $S = 10^{-8}$. The wave headings in degrees are shown in the legend with 180° head seas.

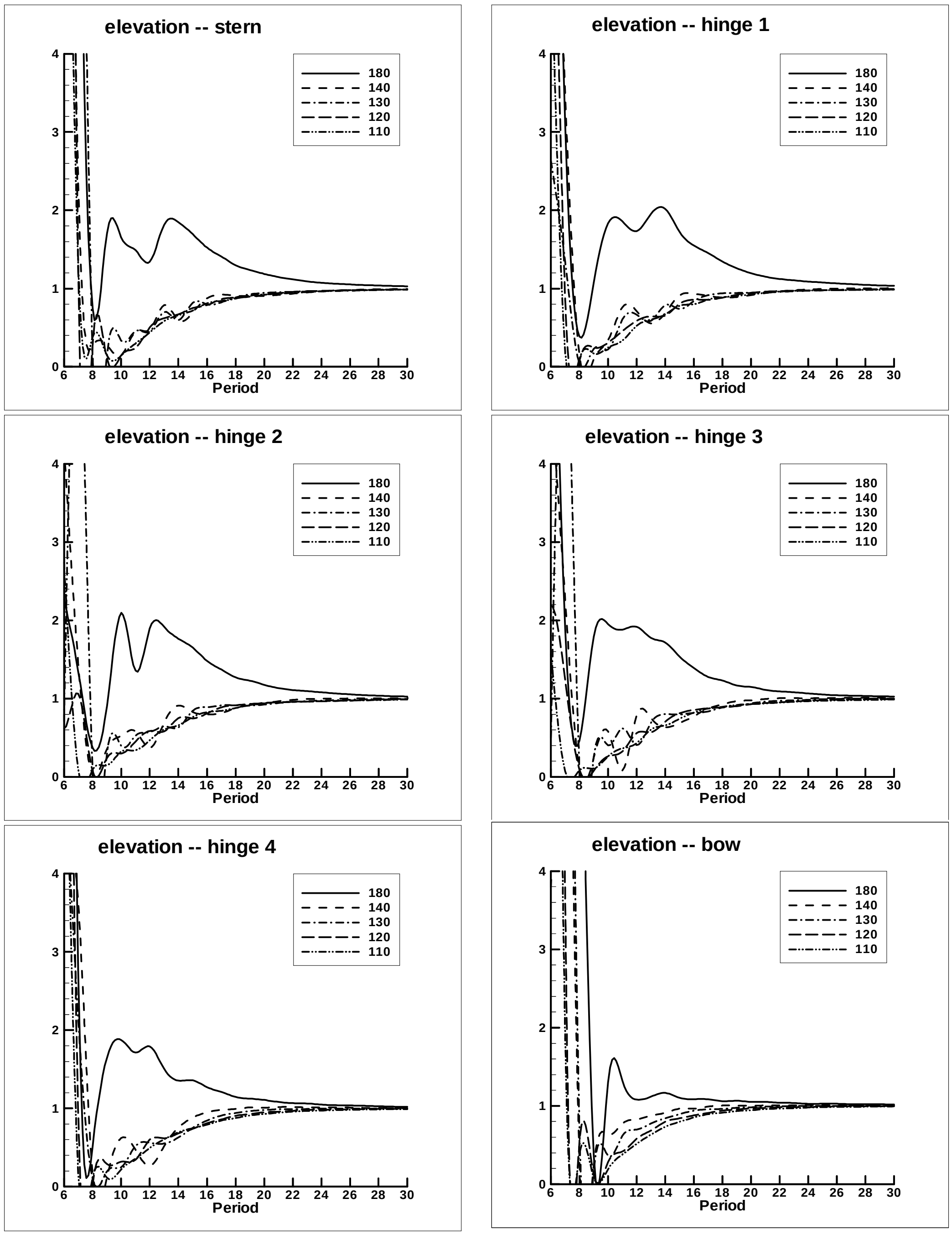

Figure 13: Elevation at the stern, hinges, and bow. Stiffness $S = 0$. The wave headings in degrees are shown in the legend with 180° head seas.

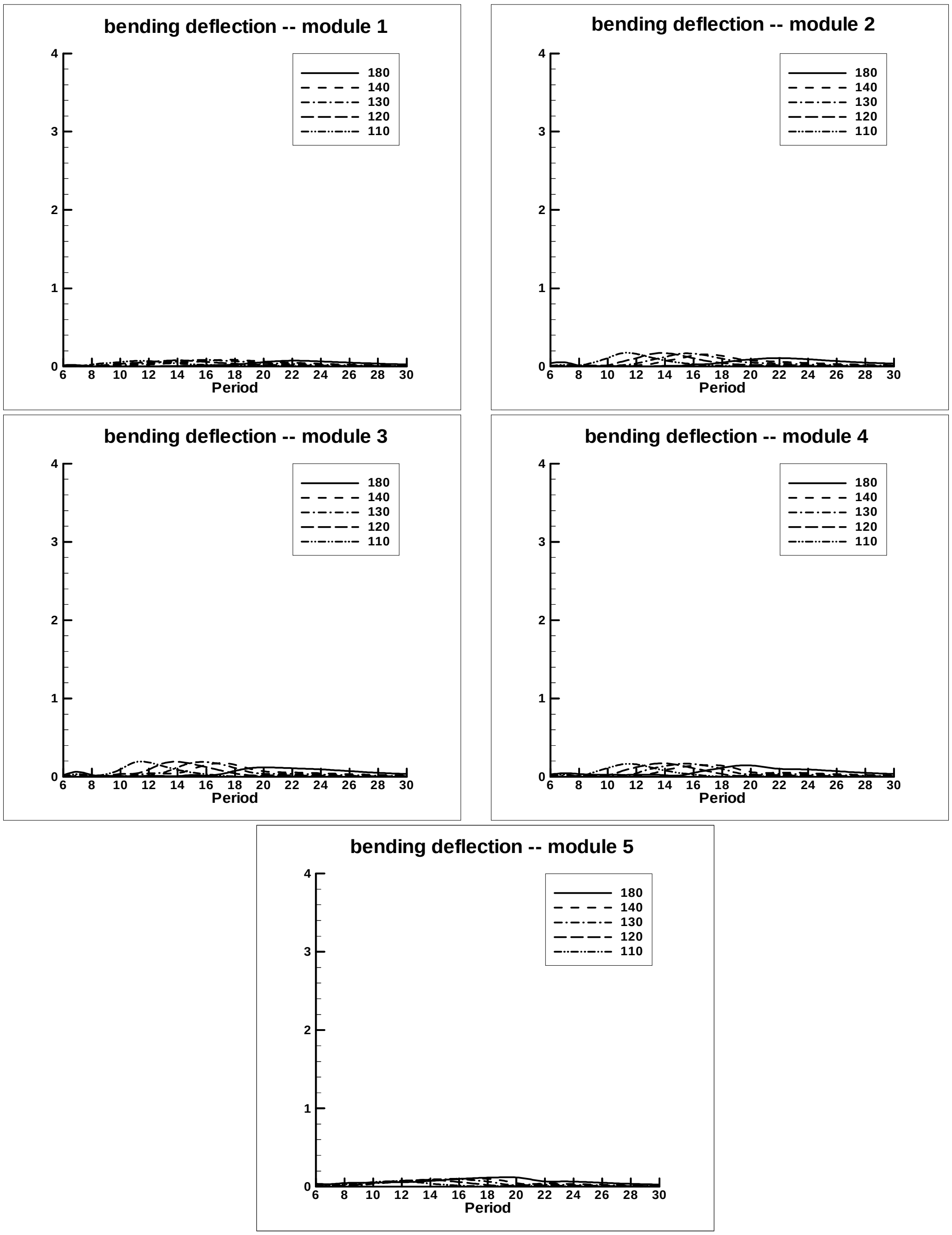

Figure 14: Bending deflection at the midpoint of each module. Stiffness $S = 10^{-2}$.

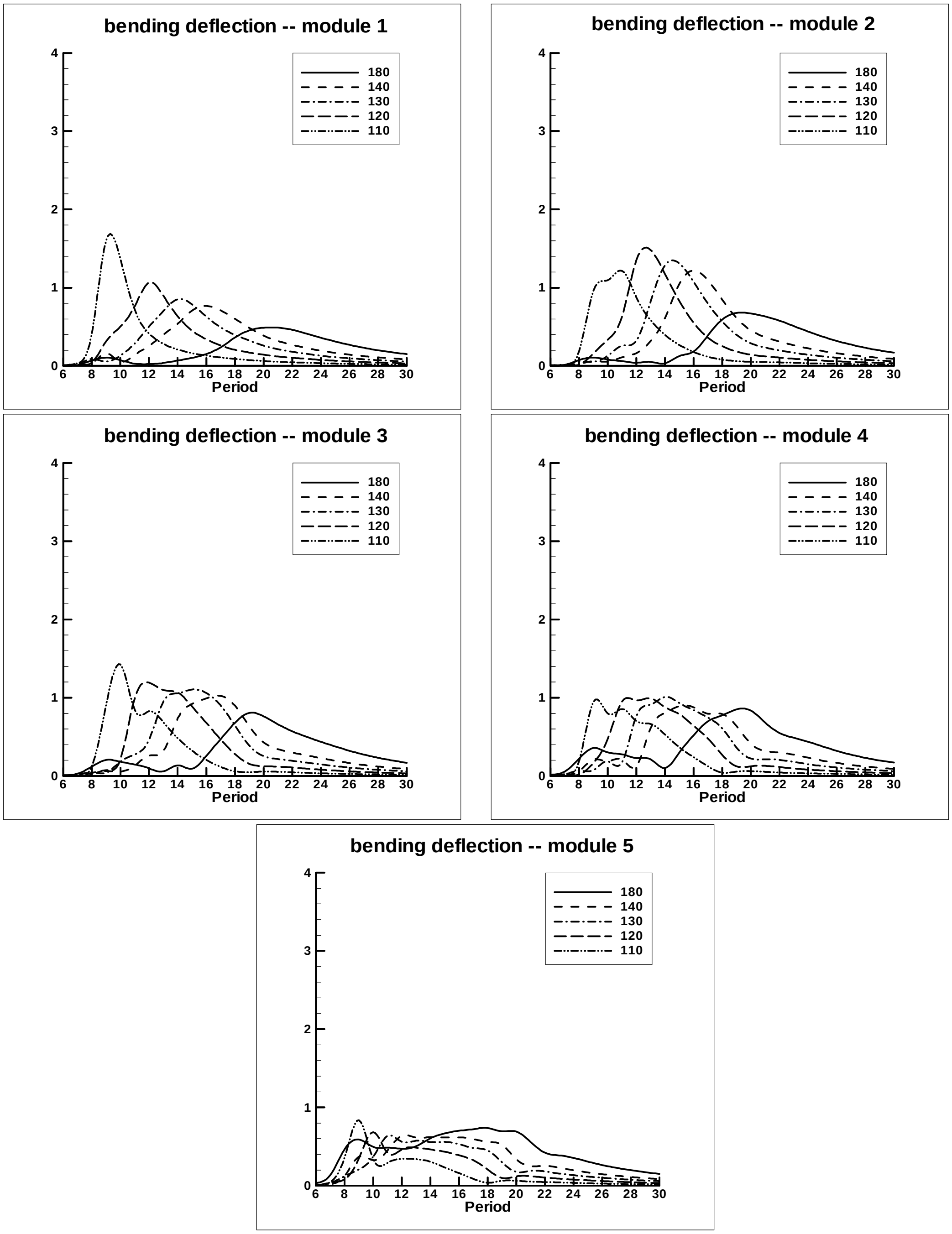

Figure 15: Bending deflection at the midpoint of each module. Stiffness $S = 10^{-3}$.

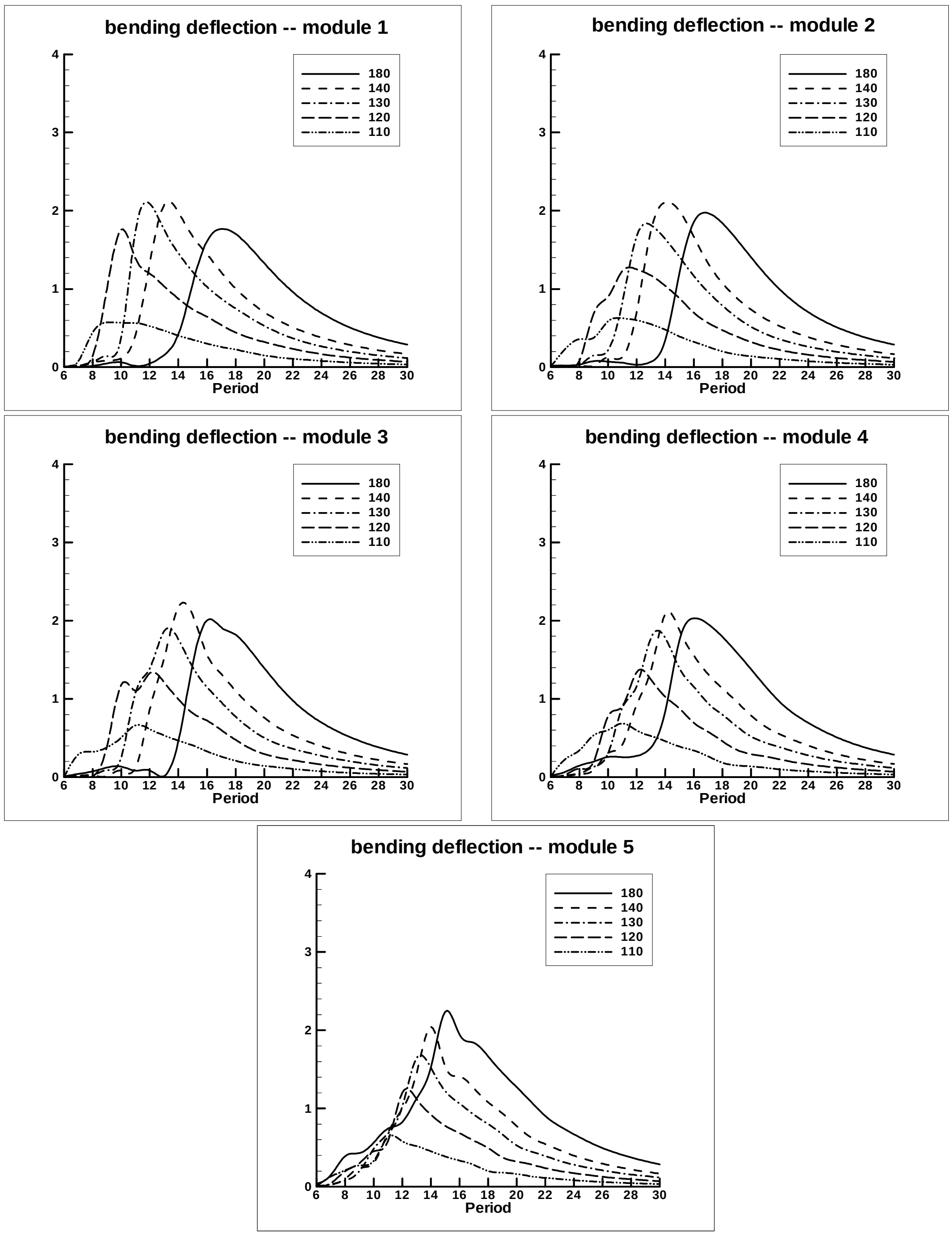

Figure 16: Bending deflection at the midpoint of each module. Stiffness $S = 10^{-4}$.

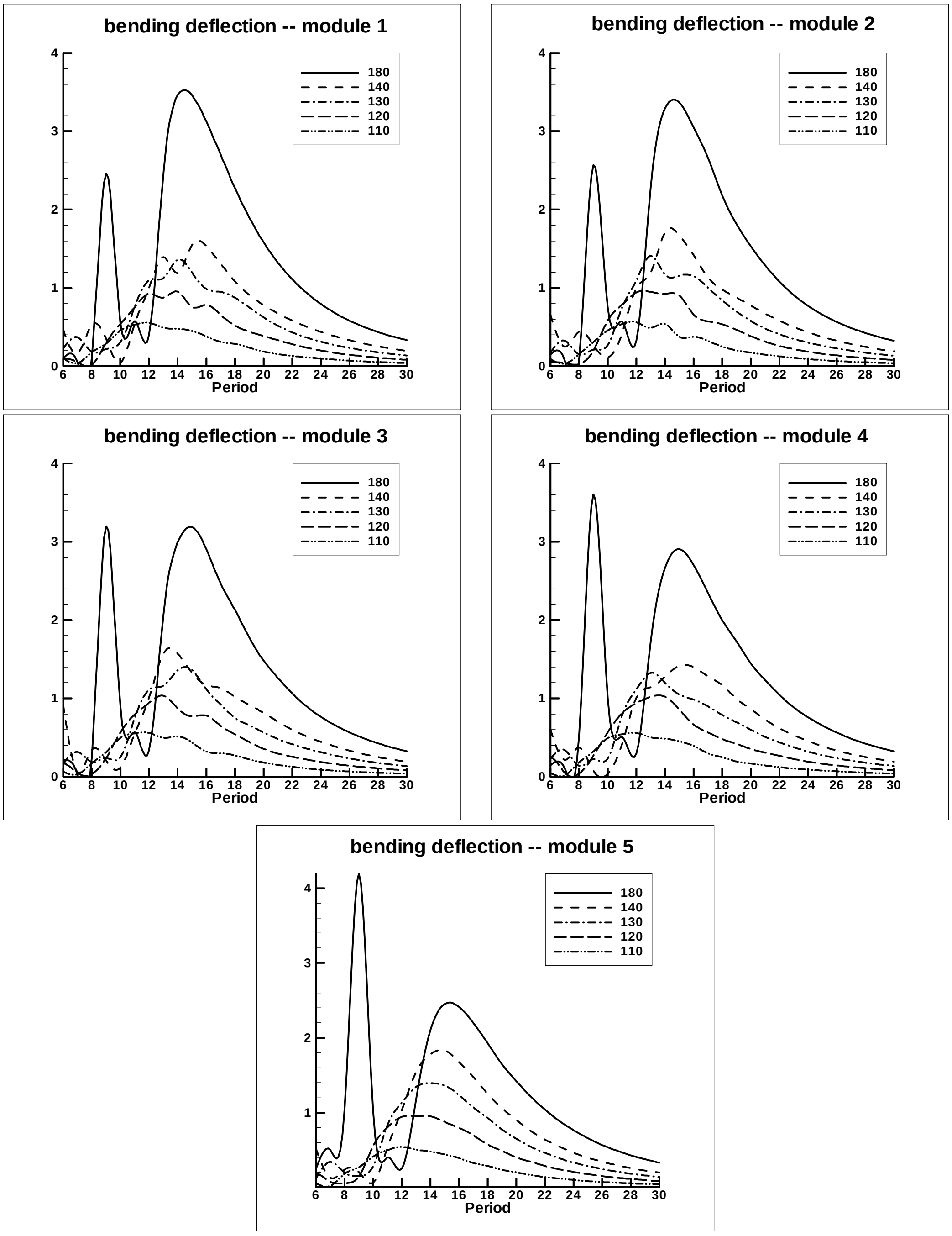

Figure 17: Bending deflection at the midpoint of each module. Stiffness $S = 10^{-6}$.

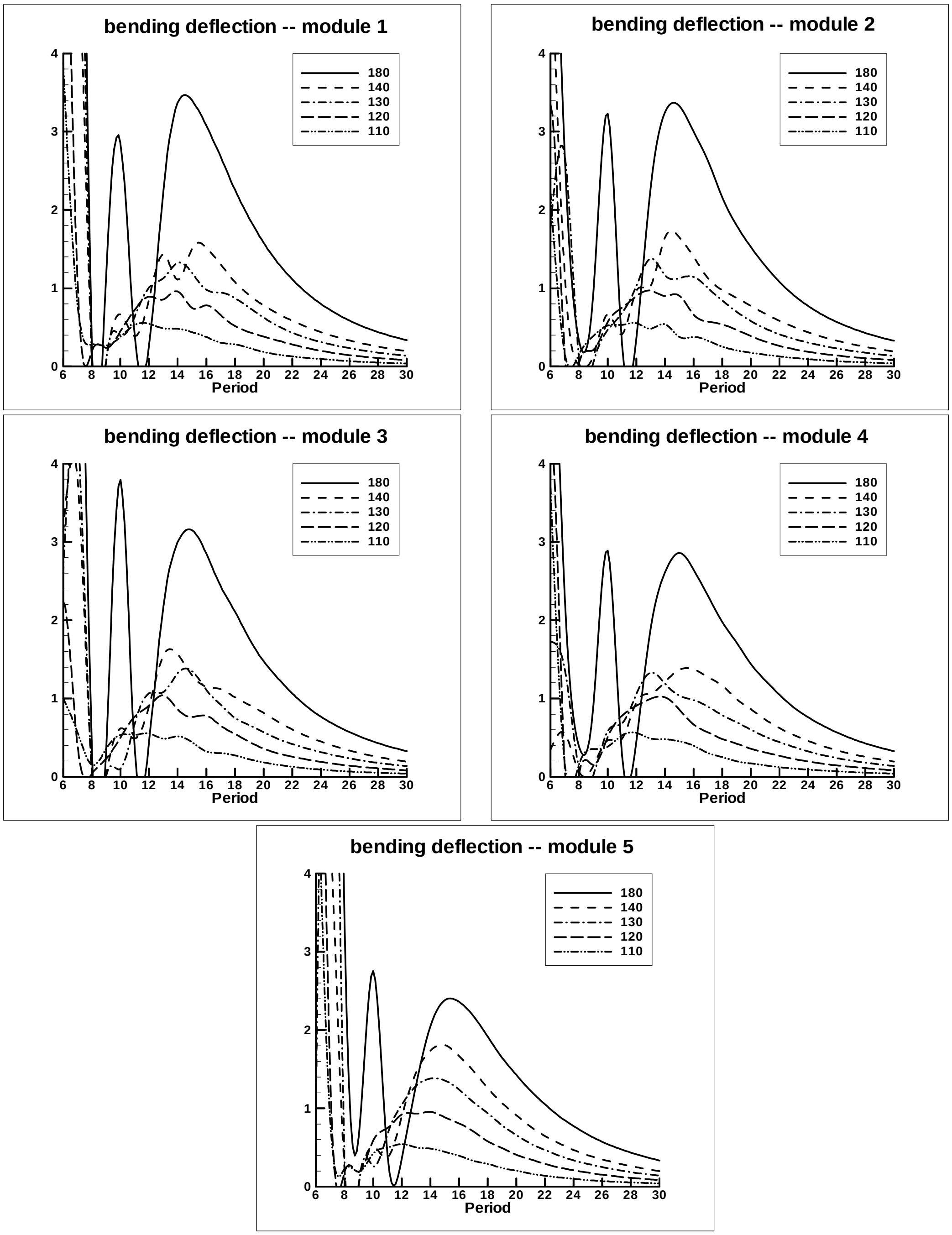

Figure 18: Bending deflection at the midpoint of each module. Stiffness $S = 10^{-8}$.

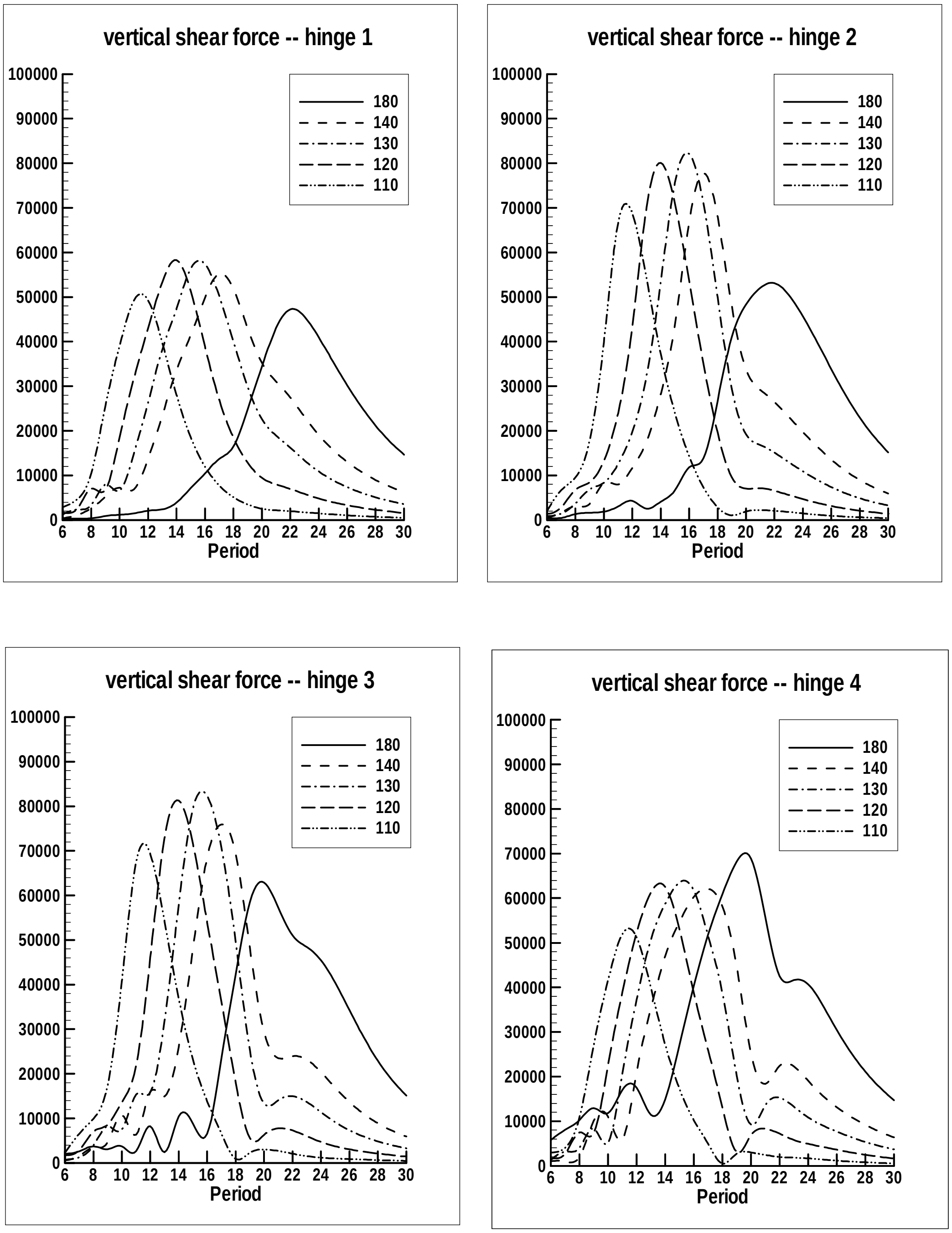

Figure 19: Vertical shear force on the hinges. Stiffness $S = 10^{-1}$.

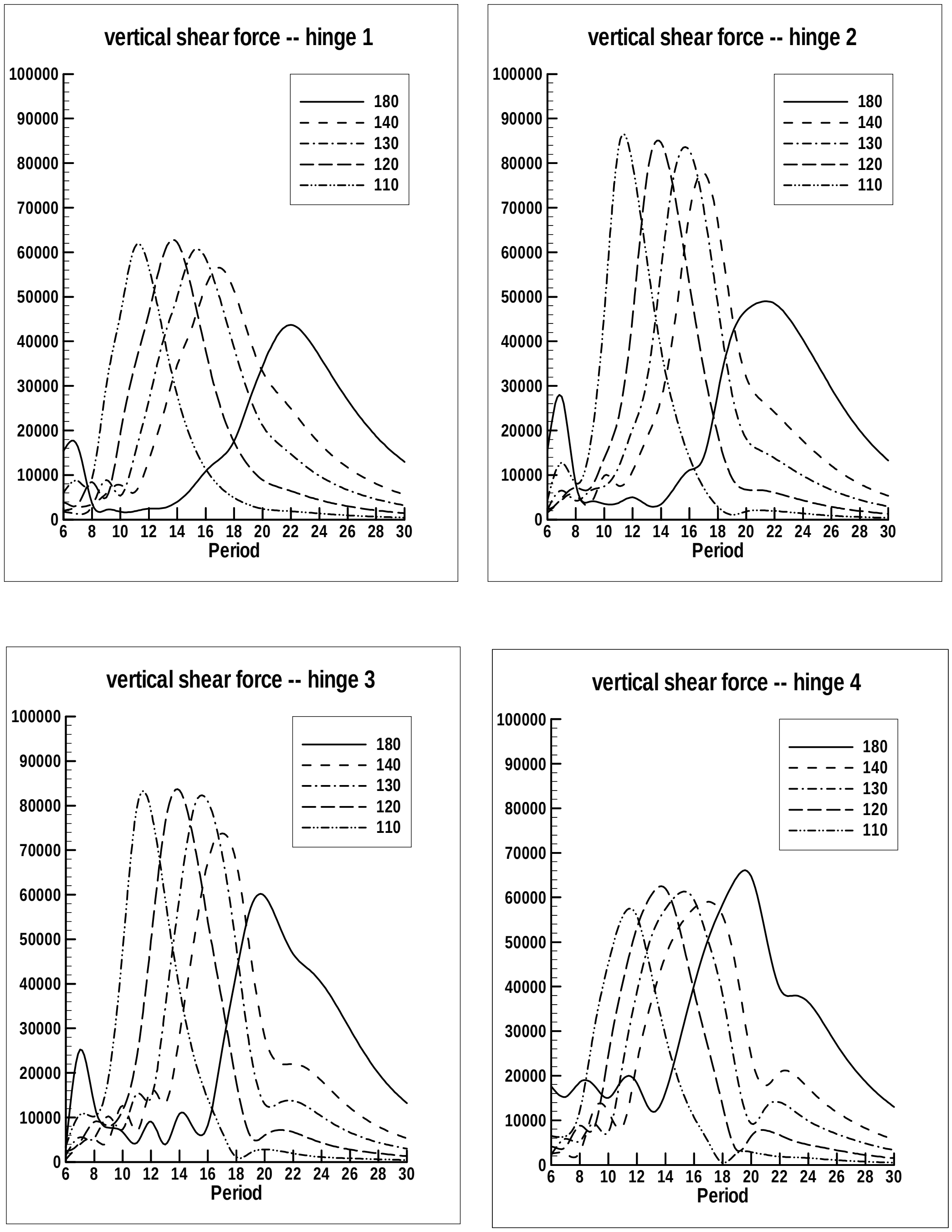

Figure 20: Vertical shear force on the hinges. Stiffness $S = 10^{-2}$.

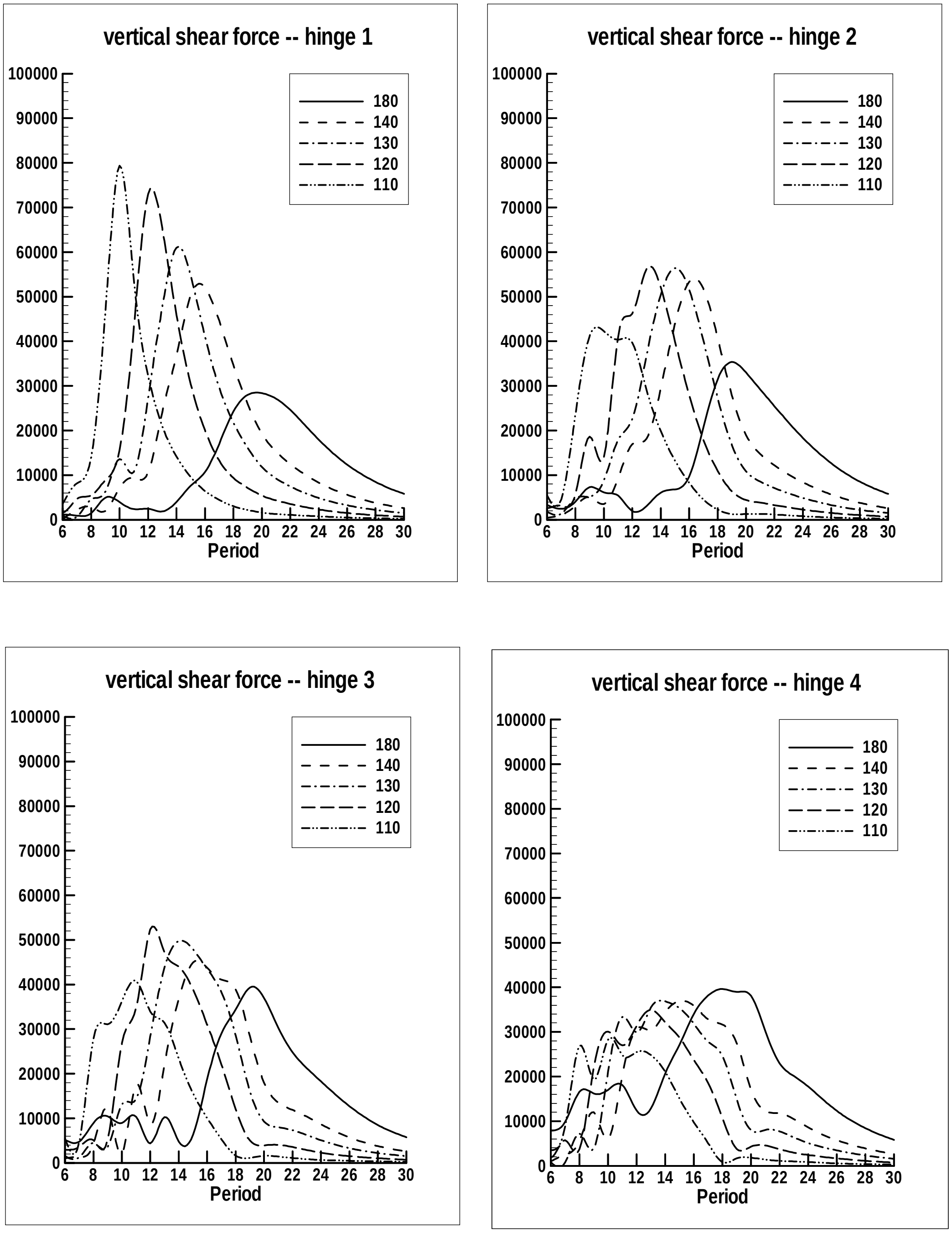

Figure 21: Vertical shear force on the hinges. Stiffness $S = 10^{-3}$.

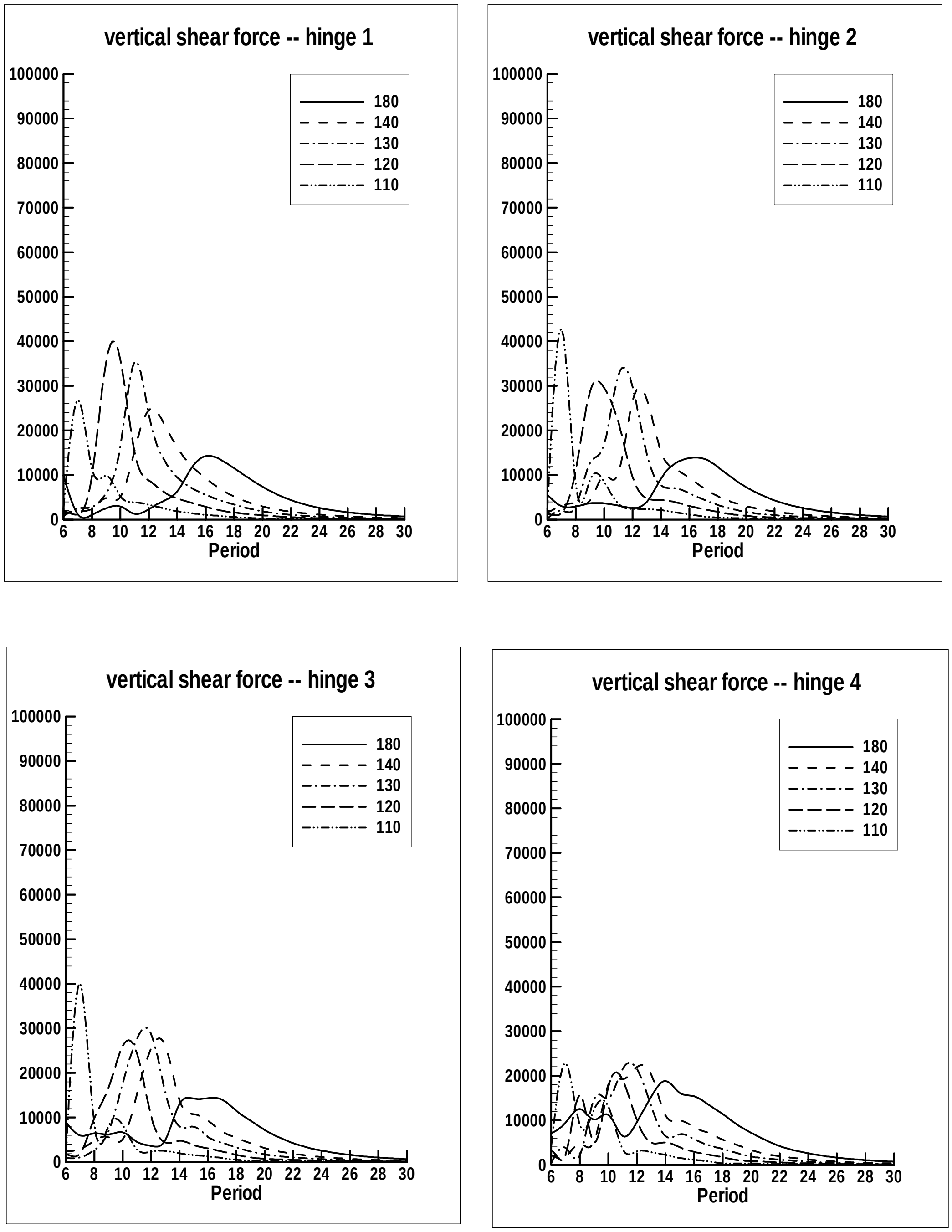

Figure 22: Vertical shear force on the hinges. Stiffness $S = 10^{-4}$.

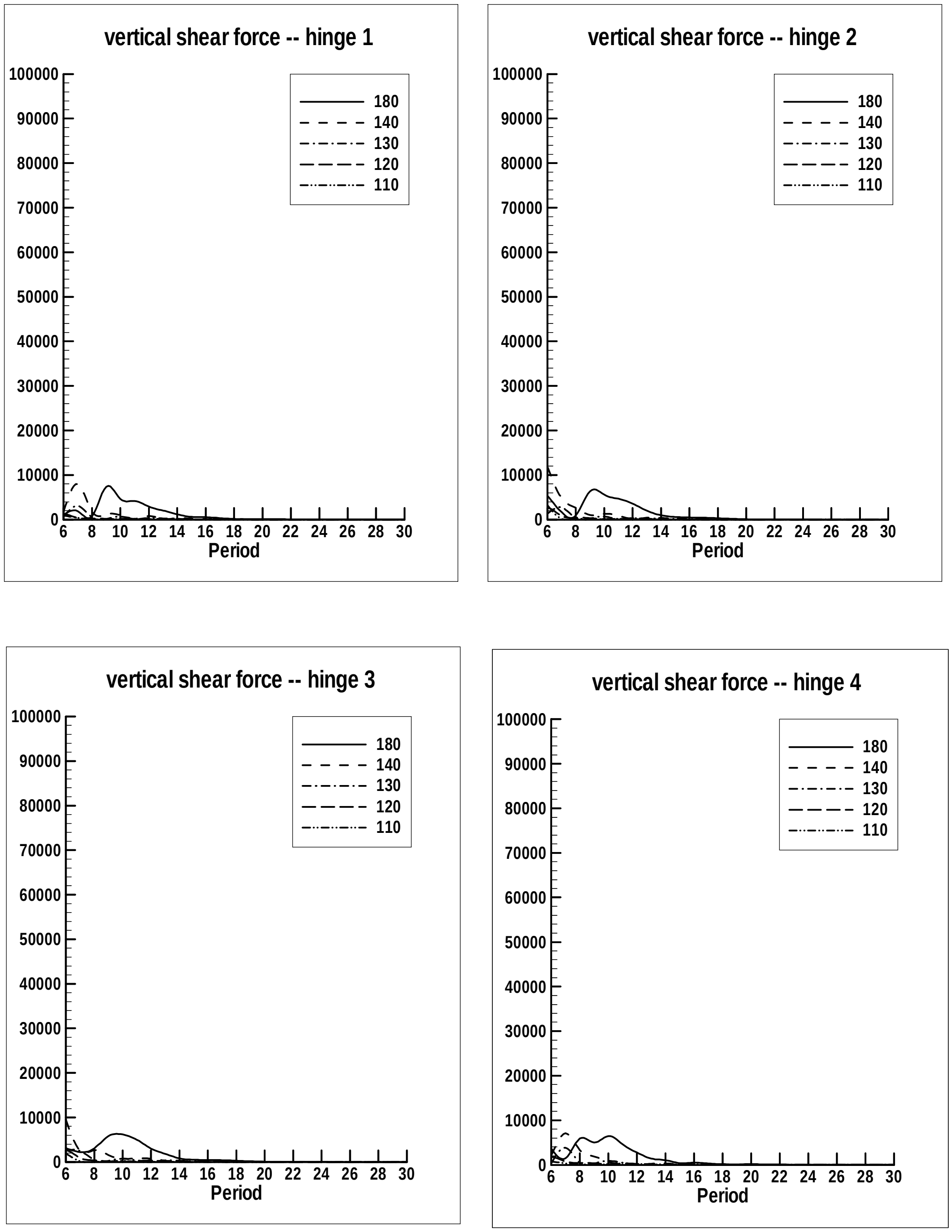

Figure 23: Vertical shear force on the hinges. Stiffness $S = 10^{-6}$.

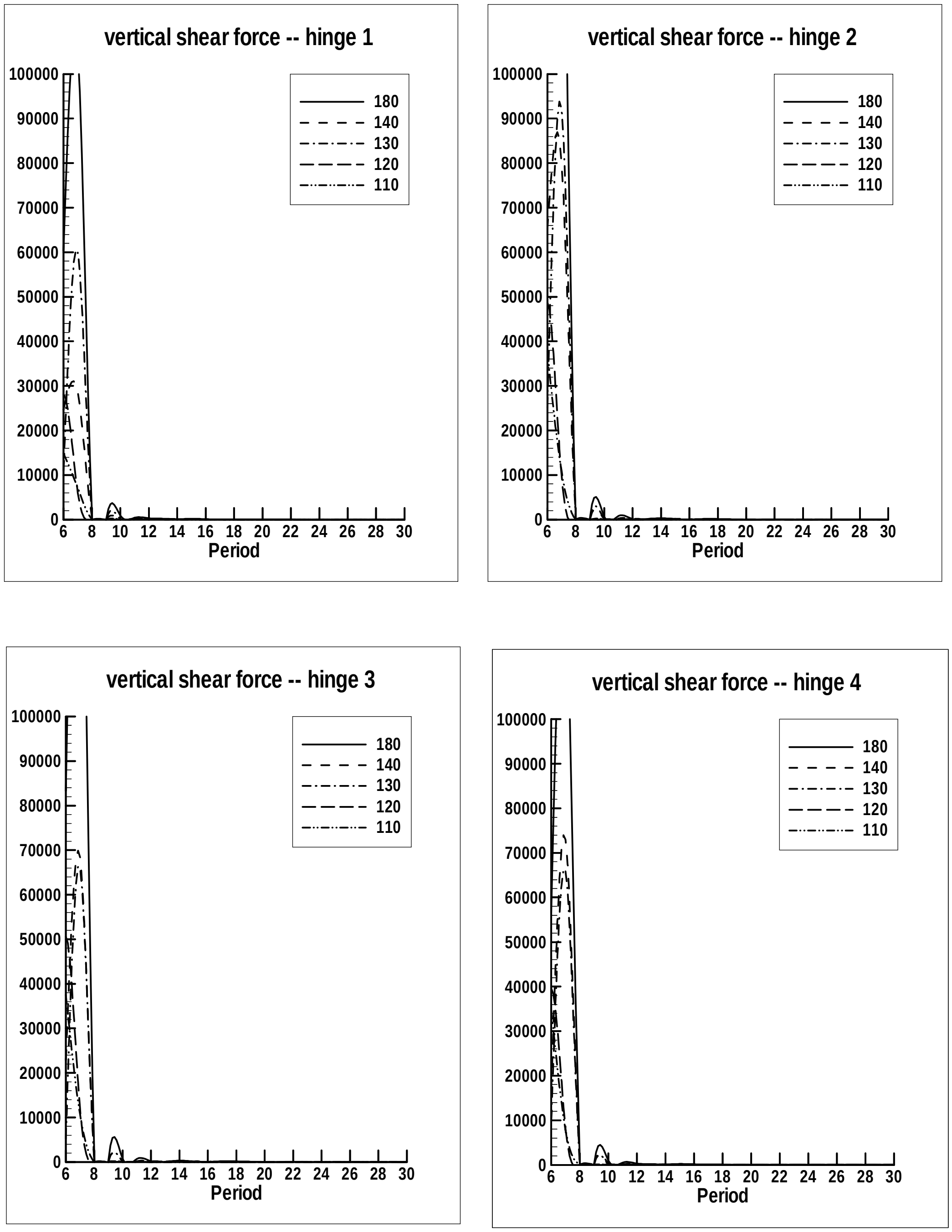

Figure 24: Vertical shear force on the hinges. Stiffness $S = 10^{-8}$.